

Interaction in Calcium Silicate Hydrates and new Composite Materials

Zur Erlangung des akademischen Grades eines
DOKTORS DER NATURWISSENSCHAFTEN

(Dr. rer. nat.)

von der KIT-Fakultät für Chemie und Biowissenschaften
des Karlsruher Institutes für Technologie (KIT)

genehmigte

DISSERTATION

von

Dipl.-Ing. Mohammadreza Izadifar

aus

Shiraz, Iran

KIT-Dekan: Prof. Dr. Manfred Wilhelm

Referent: PD Dr. Peter Thissen

Korreferent: Prof. Dr. Frank Dehn

Tag der mündlichen Prüfung: 15.04.2021



This document is licensed under a Creative Commons
Attribution-ShareAlike 4.0 International License (CC BY-SA 4.0):
<https://creativecommons.org/licenses/by-sa/4.0/deed.en>

I hereby declare that this dissertation represents the results based on my original research work from June 2018 till February 2021 in the Institute of Functional Interfaces (IFG), Karlsruhe Institute of Technology (KIT), under the supervision of PD Dr. Peter Thissen, and it has not been submitted to any another degree. All the figures and the corresponding parts of the text extracted from other references, were cited properly and faithfully.

Karlsruhe, 22.02.2021

Mohammadreza Izadifar

Contents

Abstract	iii
Zusammenfassung	v
Acknowledgement	vii
1 Introduction.....	1
1.1 Concrete.....	1
1.2 Calcium Silicate Hydrates (CSH) Phases.....	2
1.3 Corrosion of Cementitious Materials.....	3
1.4 Fabrication of Reduced Graphene Oxide from Graphite.....	5
1.5 Nanocomposite Cementitious Materials.....	7
1.6 Methods and Characterization	8
1.6.1 Simulation parameters	8
1.6.2 Model building.....	8
1.6.3 Nudged elastic band (NEB).....	9
Aims and Objectives of the Thesis.....	11
2 Correlation between Composition and Mechanical Properties of Calcium Silicate Hydrates Identified by Infrared Spectroscopy and Density Functional Theory.....	12
2.1 Characterization of Calcium Silicate Hydrate (CSH) and Calcium Silicate (CS) Phases.....	12
2.2 Calculations of Pressure and Bulk Modulus.....	16
2.3 Phases Development Process During the Hydration of Cement	18
2.4 IR Spectra of Calcium Silicate Hydrate (CSH) and Calcium Silicate (CS) Phases	19
2.5 Summary.....	22

3	Interaction of Reduced Graphene Oxide with Monomers of (Calcium) Silicate Hydrates: A First-Principles Study	23
3.1	Hydroxyl/rGO with Silicate Hydrate Moieties.....	23
3.1.1	Hydroxyl/rGO with the Si(OH) ₄ silicate hydrate unit.....	23
3.1.2	Graphene with H ₂ O and SiO(OH) ₃ for four different configurations.....	25
3.1.3	Computational models of SiO(OH) ₃ units on the graphene plane: chemisorbed and physisorbed configurations	26
3.2	Hydroxyl/rGO Combined with Calcium Silicate Hydrate Units in the Presence of Ca and Hydroxyl Groups	28
3.2.1	Hydroxyl/rGO with silicate hydrate units, in the presence of Ca.....	28
3.2.2	Hydroxyl/rGO with silicate hydrate units, in the presence of Ca involving a hydroxyl group.....	31
3.3	Epoxide/rGO with Calcium Silicate Hydrate Units.....	31
3.4	Discussions	33
3.4.1	Electronic properties of the ground-state structure with condensation reaction.....	33
3.4.2	Electronic properties of the ground-state SiO(OH) ₃ with graphene sheet.....	34
3.4.3	Electronic properties of the ground-state with condensation reaction on the addition of Ca ion	35
3.4.4	Electronic properties of the ground-state epoxide/rGO with silicate hydrate unit	36
3.5	Summary.....	37
4	Capture of Toxic Gases by Cementitious Components.....	38
4.1	CO Deposition at the Surface of Tobermorite 11 Å (004)	38
4.2	CO ₂ Deposition at the Surface of Tobermorite 11 Å (004)	48
4.3	NO and NO ₂ Depositions at the Surface of Tobermorite 11 Å (004).....	51
4.4	Summary.....	52
5	Concluding Remarks	53
	Bibliography	55

Abstract

As we know, cement is the main ingredient used to make concrete. Cement is not some sort of naturally occurring material. It is manufactured through the chemical combination of eight main ingredients during the cement production process. The eight ingredients of cement are as follows: Lime (60-65%), Silica (17-25%), Alumina (3-8%), Magnesia (1-3%), Sulfur Trioxide (1-3%), Alkaline (0-1%), Iron Oxide (0.5-0.6%), and Calcium Sulfate (0.1-0.5%). To make concrete, a mixture of Portland (10-15%), and water (15-20%) make a paste. This paste then mixed with aggregates (65-75%) such as coarse and fine aggregates. When cement is mixed with water, calcium silicate hydrate (CSH) paste is the main hydration product acting like a glue that bind coarse and fine aggregates to form concrete in any cementitious materials. Concrete and cement-based materials are the most highly used materials after water in the world. The annual production of concrete is more than 20 billion tons globally with an incremental trend of 5% per annum and contribution of 5-10% of global anthropogenic carbon dioxide emissions. It is a simple and essential material widely utilized for the construction of building, bridges, roads, public infrastructures, and dams.

In this thesis, the first research project involves simulation of eight various calcium silicate hydrate (CSH) and calcium silicate (CS) phases to measure compressibility and the resistance of the material to a uniform pressure. In the second part of this project, the optimized geometries allow for the precise calculation of vibrational eigenmodes and frequencies by the force constant approach. Four various vibration modes of stretching and bending for asymmetrical and symmetrical based on the two criteria of C/S and H/C ratios were considered to measure the wavenumber of $\nu(\text{Si-O})$. In fact, (CS) and (CSH) phases did not disclose a global trend for the wavenumber of $\nu(\text{Si-O})$ but we found that as H/C ratios increase for identical C/S ratio, the wavenumbers of $\nu(\text{Si-O})$ decrease as well.

Graphene is known as a two-dimensional material with exceptional mechanical, electrical, and thermal properties, which makes graphene-based materials excellent candidates to be used in nanocomposites. In the second research project, we employed reduced graphene oxide (rGO), which is easy to produce by the oxidation and exfoliation of graphite to be part of a calcium silicate hydrate composites (CSH), interesting for instance in cementitious materials. We studied the binding effect of rGO surface moieties, such as hydroxyl (OH/rGO) and epoxide

(Ep/rGO) groups with basic units of calcium silicate hydrates, such as silicate tetrahedra, calcium ions, and OH groups within density functional theory method. The results show that the interaction of hydroxyl/rGO with silicate tetrahedra can selectively repair the hydroxyl defects on the rGO lattice back into the graphene. Moreover, repulsion of defect from graphene sheet, and consequently condensation reaction even took place in the presence of Ca and hydroxyl groups. On the contrary, the rGO/CSH interactions remain closely to the initial structure model in the case of the Ep/rGO surface. This research fills the current gap by establishing a proper connection between the chemical composition of (CSH) units and rGO, which has revealed a wet-chemical route to obtain pristine graphene by removing hydroxyl-defects from the rGO lattice.

The third research project deals the possible storages of carbon monoxide (CO), carbon dioxide (CO₂), and moreover, nitric oxide (NO), and nitrogen dioxide (NO₂) toxic industrial gases at the surface of tobermorite 11 Å (004) within density functional theory method and FTIR measurement. Our results demonstrated that the grows of carbonate can take place at the surface of tobermorite together with the interlayer water molecule dissociation for CO deposition at the surface of tobermorite within nudged elastic band (NEB) method and FTIR measurement. We have also proofed our DFT calculation through FTIR measurement, which carbonate is formed for CO₂ deposition at the surface of tobermorite as it is exposed in the ambient atmosphere. When the carbonation is formed at the surface tobermorite 11 Å (004) for deposition of both CO₂ and CO, the only toxic gas of CO could be remained by heating up the system, and CO₂ decomposition process from carbonate is the only possible reverse reaction. It is worth mentioning that NO, and NO₂ toxic gases can be also captured by cementitious components as it was evidenced from formation of nitrate at the surface of tobermorite through DFT calculation.

Zusammenfassung

Wie wir wissen ist Zement der Hauptbestandteil der Betonherstellung. Zement ist kein natürlich vorkommendes Material. Es wird durch die chemische Kombination von acht Hauptbestandteilen während des Zementherstellungsprozesses hergestellt. Die acht Bestandteile von Zement sind wie folgt: Kalk (60-65%), Kieselsäure (17-25%), Aluminiumoxid (3-8%), Magnesia (1-3%), Schwefeltrioxid (1-3%), Alkalisch (0-1%), Eisenoxid (0,5-0,6%) und Calciumsulfat (0,1-0,5%). Zur Herstellung von Beton wird aus einer Mischung von Portlandit (10-15%) und Wasser (15-20%) eine Paste hergestellt. Diese Paste wird dann mit Aggregaten (65-75%) wie Verlaufs- und Feinaggregaten gemischt. Wenn Zement mit Wasser gemischt wird entsteht Calciumsilikathydrat (CSH) als Haupthydratationsprodukt und wirkt wie ein Klebstoff, der Aggregate unter Bildung von Beton in zementhaltigen Materialien bindet. Materialien aus Beton und Zement sind nach Wasser die weltweit am häufigsten verwendeten Materialien. Die globale jährliche Betonproduktion beträgt mehr als 20 Milliarden Tonnen mit einem zunehmenden Trend von 5% pro Jahr und einem Beitrag von 5-10% zur weltweiten anthropogenen Kohlendioxidemission. Zement wird häufig für den Bau von Gebäuden, Brücken, Straßen, öffentlicher Infrastruktur und Dämmen verwendet.

In dieser Arbeit umfasst das erste Forschungsprojekt die Simulation von acht verschiedenen Calciumsilikathydrat (CSH) und Calciumkiliat (CS) Phasen, um die Kompressibilität und die Beständigkeit des Materials gegenüber einem angelegten gleichmäßigen Druck zu messen. Die optimierten Geometrien ermöglichen genaue Berechnung von Schwingungseigenmoden und Frequenzen. Zur Messung der Wellenzahl von $\nu(\text{Si-O})$ mittels Infrarotspektroskopie (FTIR) wurden vier verschiedene Schwingungs- und Beugemoden berücksichtigt. Tatsächlich zeigten (CS) und (CSH) Phasen keinen globalen Trend für die Wellenzahl von $\nu(\text{Si-O})$, aber ein Ergebnis der Untersuchungen war, dass mit zunehmendem H/C Verhältnis für identisches C/S Verhältnis auch die Wellenzahl abnimmt.

Graphen ist als zweidimensionales Material mit außergewöhnlichen mechanischen, elektrischen und thermischen Eigenschaften. Im zweiten Forschungsprojekt setzten wir reduziertes Graphenoxid (rGO) ein, das leicht durch Oxidation und Abblätterung von Graphit

hergestellt werden kann, um Teil eines Calciumsilikathydrat-Verbundwerkstoffs (CSH) zu sein, der beispielsweise für zementhaltige Materialien interessant ist. Wir untersuchten die Bindungswirkung von rGO Oberflächeneinheiten wie Hydroxyl (OH/rGO) und Epoxid (Ep/rGO) Gruppen mit Grundeinheiten von Calciumsilikathydraten, beispielsweise Silikattetraedern, Calciumionen und OH Gruppen unter Anwendung der Dichtefunktionaltheorie (DFT). Die Ergebnisse zeigen, dass die Wechselwirkung von Hydroxyl/rGO mit Silikattetraedern die Hydroxyldefekte auf dem rGO-Gitter selektiv wieder in Graphen zurückführen kann. Im Gegensatz dazu bleiben die rGO/CSH Wechselwirkungen im Falle der Ep/rGO Oberfläche eng an das ursprüngliche Strukturmodell angelehnt. Diese Forschung füllt die derzeitige Lücke, indem sie eine korrekte Verbindung zwischen der chemischen Zusammensetzung von (CSH) Einheiten und rGO herstellt. Dies hat einen möglichen nasschemischen Weg zur Gewinnung von reinem Graphen durch Entfernen von Hydroxyldefekten aus dem rGO Gitter aufgezeigt.

Das dritte Forschungsprojekt befasst sich mit der möglichen Speicherung von Kohlenmonoxid (CO), Kohlendioxid (CO₂); darüber hinaus von Stickoxid (NO) und Stickstoffdioxid (NO₂) als toxische Industriegase an der Grenzfläche von Tobermorit 11 Å (004) unter Anwendung der Dichtefunktionaltheorie und der FTIR Messung. Die Ergebnisse zeigten, dass das Carbonatwachstum an der Grenzfläche des Tobermorits zusammen mit der Dissoziation der Wassermoleküle zwischen den Schichten für die CO Abscheidung an der Grenzfläche des Tobermorits stattfinden kann. Die DFT Berechnungen wurden durch FTIR-Messungen überprüft, wobei das Carbonat für die CO₂ Abscheidung an der Grenzfläche des Tobermorits gebildet wird, wenn dieser in der Umgebungsluft exponiert wird. Wenn Carbonat an der Oberfläche von Tobermorit 11 Å (004) zur Abscheidung von sowohl CO₂ als auch CO gebildet wird, könnte das einzige toxische CO Gas durch Aufheizen des Systems zurückbleiben und der CO₂ Zersetzungsprozess aus dem Carbonat ist die einzig mögliche Umkehrreaktion. Es ist erwähnenswert, dass auch die toxischen Gase NO und NO₂ durch zementhaltige Komponenten abgefangen wurden.

Acknowledgement

First of all, I would like to thank to the Almighty Lord for always blessing and supporting me.

I would like to thank my supervisor PD Dr. Thissen for giving me the opportunity to conduct this PhD work in his working group and supporting me all the time.

During these three years, I have met several people that have contributed to my personal and academic development. I also traveled to Materials Physic Center (CFM) institute located in Donostia-San Sebastian for duration of six months supporting by Karlsruhe House of Young Science (KHYS). I would like to give them the acknowledgement they deserve.

I would like to thank Prof. Dr. Wöll, head of the institute of functional interface (IFG) for supporting me and giving me the opportunity to conduct my PhD work in his institute.

I would like to thank Prof. Dr. Gerdes for supporting me and holding high quality meetings during these three years.

I would like to thank Virtmat team under supervision of Prof. Dr. Wenzel from INT institute for holding high quality workshops and meetings during these three years.

I would like to thank Karlsruhe House of Young Science (KHYS) for the financial support for duration of six months to expand my research study in Materials Physic Center (CFM) institute in Donostia-San Sebastian.

I would like to thank Dr. Dolado and Dr. Ayuela from CFM, who were willing to teach and guide me all the time in Materials Physic Center (CFM) institute.

I would like to thank PD Dr. Böttcher, who supported me for three semesters working in lab to supervise bachelor and master students.

I would like to thank Mr. Königer, who supported me all the time with everything, specially to solve the problems occurred with my PC.

I would also like to thank Ms. Mohammadi Hafshejani for helping me during my PhD work.

Chapter 1

Introduction

1.1 Concrete

After water, a man-made material called concrete is widely utilized on Earth. It is a significant material, broadly exerted for constructions of roads, bridges, dams, buildings, and public infrastructures [1]. Worldly, concrete is annually produced by more than 20 billion tons with contribution of 5–10% of the carbon dioxide production [2, 3]. Concrete is comprised of cement, aggregates (coarse and fine), water and chemical admixture [4]. In fact, when cement mixes with water, a glue consisting of many phases are produced that binds coarse and fine aggregates to form a composite material of concrete [5]. To improve the service life of concrete, durability increment, permeability reduction and a longer affective lifetime of concrete are needed. In other words, concrete failure can be caused by many reasons, such as thermal cycling, reinforcement corrosion, and permanent dynamic stresses caused by frequently passing vehicles [1]. In fact, water permeability through concrete component can cause corrosion of concrete surface resulting the exposure of reinforcement in the ambient atmosphere, and consequently reinforcement corrosion. Hence, a thorough examination from atomic scale concerning reaction of cement with water [2, 6-11] must be carried out to increase the service life the concrete, and reduce the environmental impacts [12].

1.2 Calcium Silicate Hydrates (CSH) Phases

The interaction of calcium silicate (CS) phase with water can be taken into account as the most significant aspect [13]. As shown in Figure 1.1, hydration of cement with water can be determined by a sequence of chemical reactions (production of (CSH) phases) resulting binding the material [14]. In fact, any modification of concrete properties must be carried out at the atomic scale and during hydration of cement. Hydration of cement resulting production of calcium silicate hydrate (CSH) [15] gel acting like a glue to bind the coarse and fine aggregates in cement-based materials. Calcium silicate hydrate gel is determined as the major component of concrete [16], which roughly contains 60 percent of hydration products [17]. It is also worth mentioning that the mechanical properties of the cement-based construction materials is controlled by the (CSH) phases, which are fabricated during hydration of cement [15, 17, 18]. The complexity of the (CSH) [19-21] structure can be ascribed to the interlayer of water, the layered material structure at the nanoscale [22, 23], the globular texture at the mesoscale [24-26], and the multi-scale porous structure [27-29].

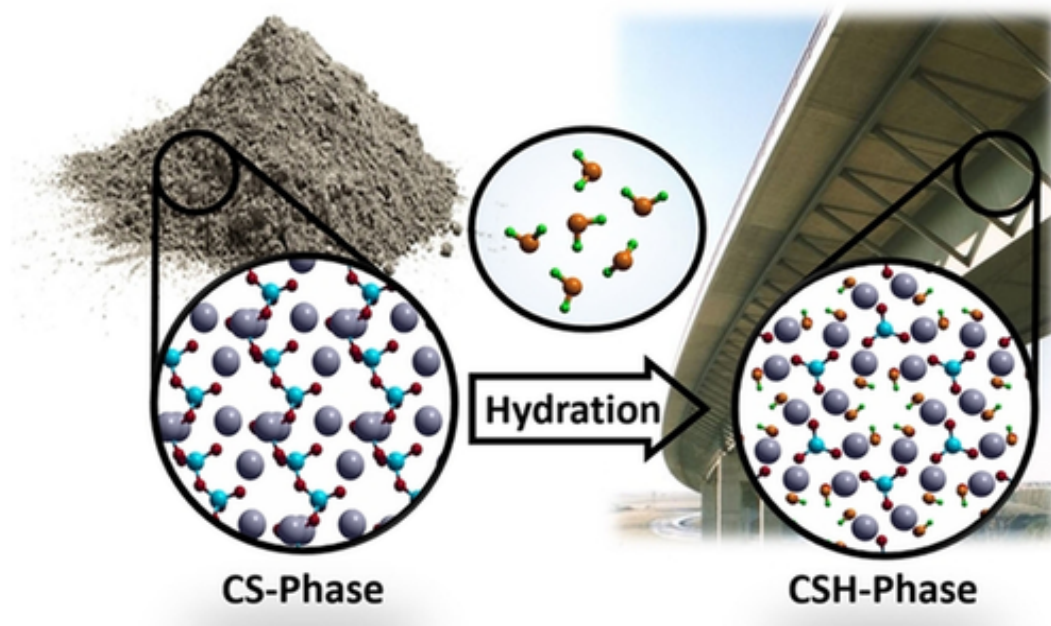


Figure 1.1: Hydration of (CS) phase found in cement resulting production of (CSH) phases for binding material. Reprinted with permission from [30]. Copyright (2018) John Wiley & Sons.

In reality, better comprehension of mineral surface chemistry and its reaction with water are needed for porous materials in order to stop corrosion by the time. The possible and best known reaction that leads to corrosion of (CSH) and (CS) phases is the metal proton exchange reaction (MPER) as is explained in the next section [13, 31].

1.3 Corrosion of Cementitious Materials

These days, degradation of concrete is a principal concern for developing countries. The failure of concrete-based construction can be caused by many reason, such as reinforcements corrosion, temperature changes during day/night, and mechanical stress caused by vehicles; however, the direct interaction of (CSH) and (CS) phases with aqueous or humid environments are considered as the substantial problems resulting breaking up the silicate chain at the surface region of concrete.

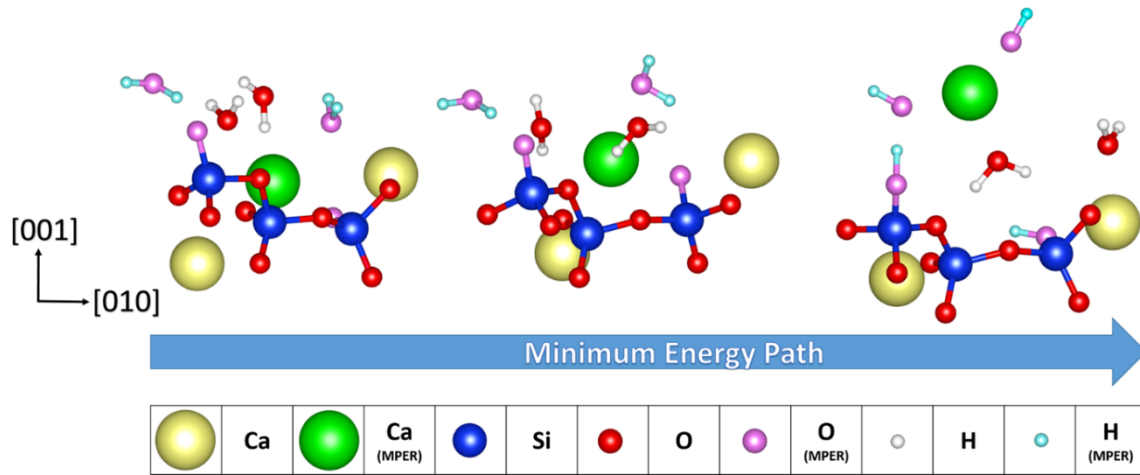


Figure 1.2: Metal-proton exchange reaction (MPER) on the wollastonite (001). Reprinted with permission from [13]. Copyright (2016) The Journal of Physical Chemistry C.

Corrosion of cementitious material through MPER can lead crystalline phase transformation to glassy (CSH) phases. As can be observed from Figure 1.2, the MPER on wollastonite can cause the removal of Ca ion from the structure, and therefore the oxygen (pink color) coordinated to silicon is protonated by water; finally, the shape of crystal is modified again. It is also worth mentioning that the length of the silicate tetrahedra chain plays a significant role in the mechanical properties and also specifies how MPER can affect the structure. In fact, leaching of metal ions into the environment through the MPER resulting immense structural changes concerning (CSH) and (CS) [14]. Giraudo et al. [13] demonstrated that the MPER on model system of wollastonite leads to a critical structural changes of the micrometer-sized particles in hydrous environment. Oelkers et al. [32] also studied the MPER on various minerals and finalized that the number of protons used through this exchange reaction is mineral specific. The below equation can demonstrate the MPER as Ca leaches into the ambient and OH groups formation at the surface by proton exchange between water and mineral [13, 30, 32, 33].



1.4 Fabrication of Reduced Graphene Oxide from Graphite

Graphene [34] is a two-dimensional metrical (honeycomb sp^2 carbon plane), which has obtained researchers attention to be employed in some important applications, such as composite materials [35, 36] energy storage devices [37], and electronic devices [38], because of its unique thermal [39-42], electrical [43], mechanical [44, 45], and chemical properties [46-49]. In fact, significant challenge of high quality graphene fabrication through a low cost method has been remained as a gigantic challenge[48]. Graphene can be fabricated through two ways, such as chemical vapor deposition (CVD) [50, 51] or exfoliation of graphite and growing on the various substrates epitaxially [34, 50, 52]. The CVD method is considered as a less cost-effective approach for fabrication of graphene because it involves costly equipment and high temperature procedures with very surface defects. Therefore, exfoliation of graphite and reduction of surface functional groups by chemical, thermal or electrochemical reduction methods into reduced graphene oxide (rGO) attracted attention of researchers due to compatibility of solution-processing these days [53, 54].

Graphite oxide is fabricated through the oxidation of graphite according to the most extensively technique of classical Hummer's method [52, 55-57]. As a matter of fact, graphite oxidation treatment is a feasible aid for raising the distance between the graphene planes by the presence of oxygen functional groups, such as epoxide, hydroxyl, carbonyl, and carboxyl groups for a simpler exfoliation [54]. On the other hand, graphite oxide exfoliation is also considered as a considerable intermediate procedure for fabrication of graphene oxide from graphite. Graphite oxide is thoroughly exfoliated into graphene oxide through two procedures of either mechanical stirring method by the water/graphite oxide mixture for a long sufficient time [58] or ultrasonication method in a polar organic solvent or aqueous media [47, 59]. The plane of fabricated graphene oxide plane is highly populated with either hydroxyl or epoxide functional groups while the edge of the plane is mainly occupied by few carboxyl and carbonyl groups. These oxygen functional groups of epoxide and hydroxyl can be taken into account as the surface structural defects of the graphene layer, as illustrated in Figure 1.3. Therefore, in the third chapter of this dissertation, we will perform a comprehensive study for the interaction mechanism of (CSH) with rGO surface populated with epoxy or hydroxyl functional groups (Figure 1.3 below, left and right) [60] for fabrication of nanocomposite cementitious materials.

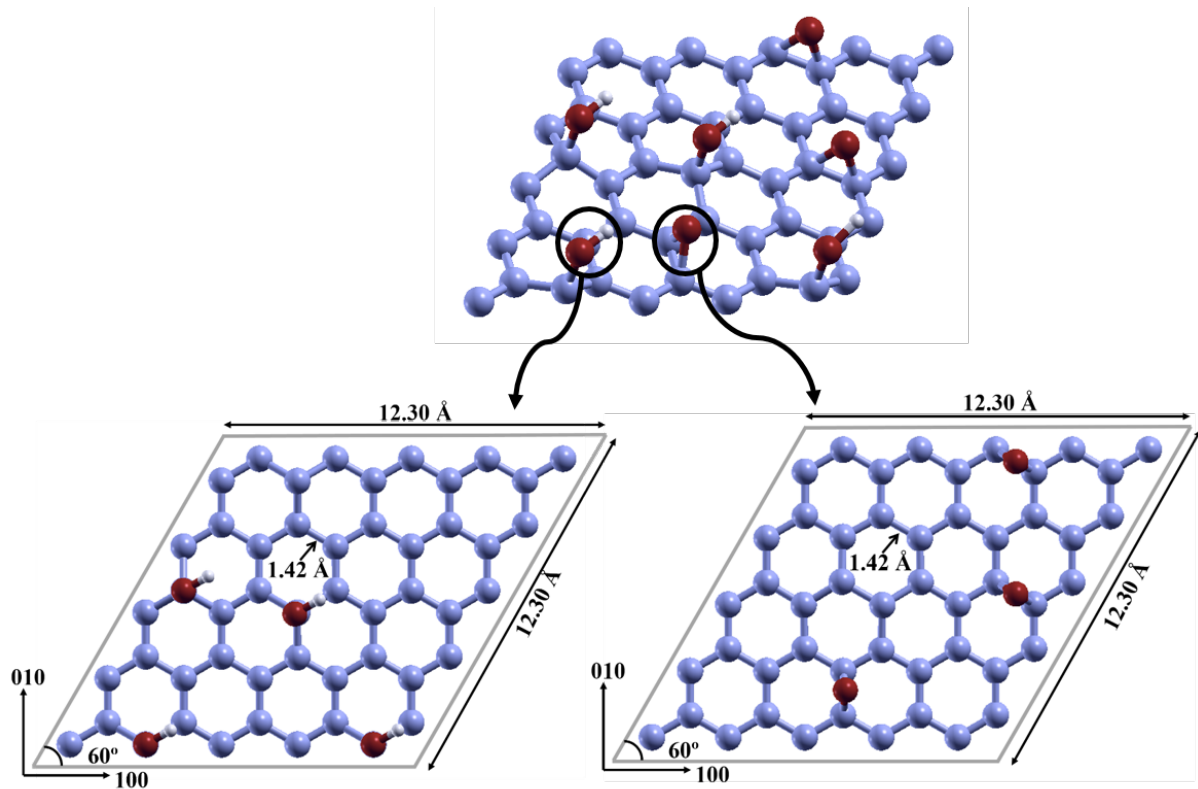


Figure 1.3: Reduced graphene oxide (rGO) populated with surface functional groups of hydroxyl and epoxide. Below, left and right panels show reduced graphene oxide with hydroxyl and epoxide surface functional groups, respectively.

Lately, many studies have been performed to manufacture rGO with low density of epoxide and hydroxyl surface functional groups [54]. Feng et al. fabricated rGO with the lowest contribution of oxygen functional groups of 5.6 wt% by using Na-NH₃ treatment through active solvated electrons as the highly reductive agent [61]. Liao et al. [62] fabricated graphene from exfoliated GO in DI water at pH \approx 3 within 12 and 48 hours at the temperatures of 120 and 95 °C with the ratio reduction of oxygen to carbon to about O:C = 1:6 by C^{1s} XPS spectra measurement, respectively. Moreover, Pei et al. [63] carried out the reduction of GO films into highly conductive and flexible graphene films by a HI acid solution, 85% N₂H₄·H₂O solution and 50 mM NaBH₄ aqueous solution by liquid immersion at room temperature. Their observations revealed that after reduction by HI acid, the majority of oxygen containing groups in GO film were eliminated and C-C bonds became dominant with C/O atomic ratio above 12 and electrical conductivity as high as 298 S/cm, much higher than those of the GO films reduced by NaBH₄ and hydrazine.

1.5 Nanocomposite Cementitious Materials

We earlier evidenced that any modification for cement-based construction materials must be performed during hydration of cement and before hardening of the (CSH) paste. To the best of our knowledge, no studies within DFT calculation (atomistic scale) have been performed to examine the interaction mechanism of rGO surface populated with epoxy or hydroxyl functional group with (CSH) gel to fabricate nanocomposite cementitious materials for further modification of the mechanical properties of cement-based construction materials. In contrast, some researches have been experimentally carried out to fabricate composite concrete material consisting of GO or rGO. For instance, Li et al. [64] reported that GO can increase the compressive strength of cement pastes by 42.3, 43.4, 48.5, and 56.3% for contribution of GO dosages of 0.02, 0.04, 0.06, and 0.08 at 28 days, respectively. Gong et al. [65] also reported that the utilization of 0.03% by weight GO sheets into the cement paste can enhance the tensile strength and compressive strength of the cement composite by almost 40% because of pore reduction of the cement paste. Recently and in 2020, Jyothimol et al. [66] used ordinary Portland cement with grade of 53 for fabrication of composite cementitious system with rGO in the form of powder experimentally. They found that compressive strength of concrete can be increased by 100-113% for the early age of 3 days. It is also reported that the workability of rGO modified concrete decreased and it can be ascribed to the formation of agglomerated structure. We also simulated calcium silicate hydrate composites consist of (CSH) gel and epoxide/rGO as shown in Figure 1.4.

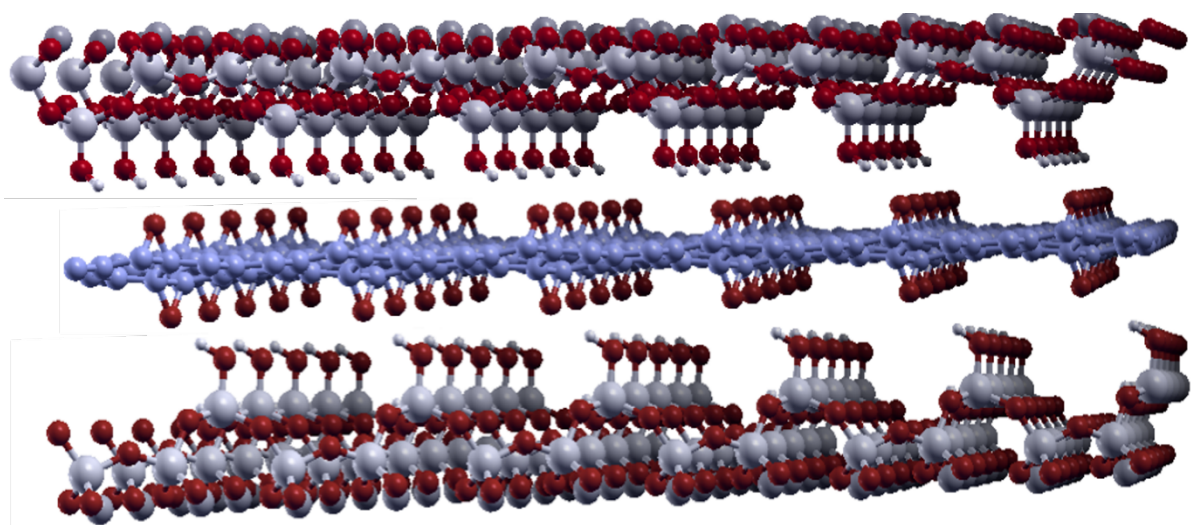


Figure 1.4: Calcium silicate hydrate composites consist of (CSH) gel and epoxide/rGO.

1.6 Methods and Characterization

1.6.1 Simulation parameters

The DFT was employed as defined in the Vienna ab initio simulation package (VASP) [67-70] for the calculation of the electronic structure. The Perdew–Burke–Ernzerhof (PBE) functional was employed to describe the electron exchange and correlation energy within the generalized gradient approximation [71]. The projector-augmented wave method [72] and pseudopotential were used to describe the electron–ion interaction. A plane wave up to a kinetic energy cutoff of 400 eV was defined for the DFT calculations. The Brillouin zone sampling was carried out with $1 \times 1 \times 1$, $2 \times 2 \times 1$, and $3 \times 3 \times 1$ meshes of Monkhorst–Pack k-points for the calculations regarding first, second and third projects, respectively [73]. The density of state (DOS) regarding the second project in the third chapter also was calculated with a refined mesh of $34 \times 34 \times 1$ Monkhorst-Pack k-points. Charge transfers were calculated using the Bader analysis, with a code developed by Henkelman and co-workers [74]. The optimization of the atomic coordinates (and unit cell size/shape for the bulk materials) was performed through a conjugate gradient technique, which utilizes the total energy and the Hellmann–Feynman forces on the atoms (and stresses on the unit cell). The structures were considered to be fully relaxed when the forces on the atoms were smaller than 0.01 eV \AA^{-1} . Vibrational eigenmodes and frequencies were calculated by the force constant (FC) approach [75]. We also used open-source XcrySDen software, which is a crystalline and molecular structure visualization program to display the crystalline structure and electron densities [76].

1.6.2 Model building

Regarding the first project as described in the second chapter, we developed optimized primitive unit cell of eight hydrated phases as model systems compatible with the phases created during the hydration of cement: tobermorite 14 \AA , 11 \AA , and 9 \AA , Wollastonite, Jaffeite, Jennite, $\gamma\text{-C}_2\text{S}$, and $\alpha\text{-C}_2\text{SH}$ according to table 1 published by Richardson et al [22].

Regarding the second project as described in the third chapter, we developed models of reduced graphene oxide (rGO) looking at hydroxyl or epoxide groups with periodic boundary conditions along x and y directions to remove finite length effects, and a vacuum slab with a thickness of 10 \AA well converged to avoid the interactions with adjacent cells in the z direction.

Larger boxes of 15 Å were also tested in some cases involving rGO, Ca and silicate units, and the calculated energy differences were found to be converged below meVs. Thus, the optimized primitive unit cell of rGO was characterized by the following parameters $a = 12.30$ Å, $b = 12.30$ Å, $c = 10$ Å, and $\alpha = 90^\circ$, $\beta = 90^\circ$, $\gamma = 60^\circ$. We considered silicate hydrate moieties taken as $\text{Si}(\text{OH})_4$ monomers because they appear in solutions when calcium silicates are hydrated in cementitious materials. Furthermore, we studied $\text{SiO}(\text{OH})_3^-$ units that are obtained in a small quantity during the hydration process and are responsible for the raise in pH found in cements. It is also worth mentioning that the contribution of van der Waals (vdW) interaction for all configurations in this studied were neglected due to the small calculated vdW potential energy in some tests. The ΔE is calculated from the energies difference between the relaxed expected configuration and ground-state structure. For our simulation models in this study, we have selected the reduced graphene oxide structures with the ratio reduction of oxygen to carbon to $\text{O}:\text{C} = 1:50$.

Regarding the third project as described in the fourth chapter, the optimized primitive unit cell of tobermorite 11 Å (004) was characterized by the following parameters $a = 6.73$ Å, $b = 7.37$ Å, $c = 22.68$ Å, and $\alpha = \beta = 90^\circ$, $\gamma = 123.18^\circ$ [77]. We developed models of tobermorite 11 Å (004) with periodic boundary conditions along x and y directions to remove finite length effects, and a vacuum slab with a thickness of 23 Å well converged to avoid the interactions with adjacent cells in the z direction. The contribution of van der Waals (vdW) interaction for all configurations in this studied were neglected. It is also worth reporting that we activated spin-polarization for our calculations in this study.

1.6.3 Nudged elastic band (NEB)

The Nudged Elastic Band (NEB) method can be employed to find a reaction path and the transition state between a reactant and a product state as shown in Figure 1.5. At the beginning of a NEB calculation, the geometry of the initial and final systems are optimized to minimize their energy. Then a rough approximation of the reaction path is build: a set of image is created by performing a liner interpolation between the initial and final systems. An intermediate system can be provided, in which case the interpolation is performed between the initial and intermediate systems, and then between the intermediate and final systems.

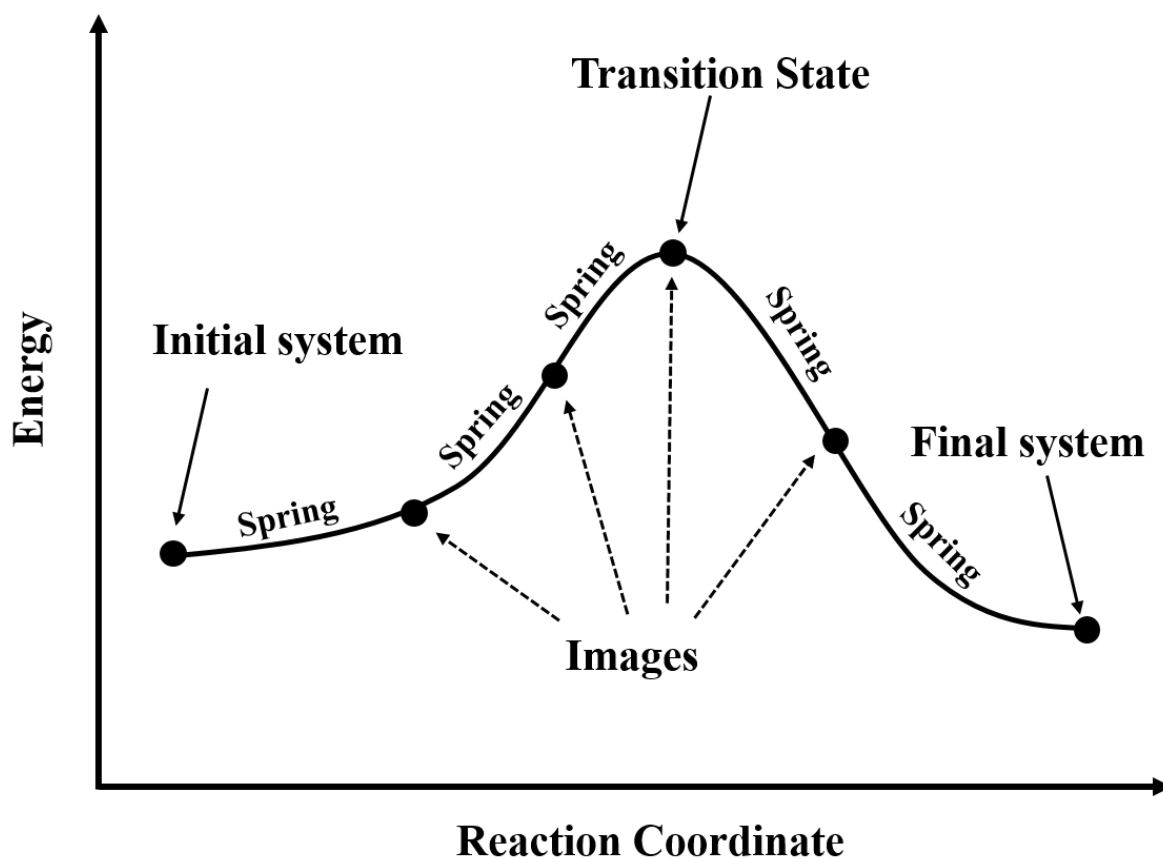


Figure 1.5: A minimum reaction path calculated through NEB.

Finally, a reaction path is found by performing within a simultaneous optimization of all images. In the NEB method the images are not dependent from each other. The force on each image depend on its neighboring images: at each step the force parallel to the reaction path are eliminated and a so-called spring force is added tries to keep each image in the middle between its neighbors. This does not let images slide to the initial or final reaction state and ensures that they are evenly distributed along the reaction path.

Aims and Objectives of the Thesis

The aims of this thesis involves with the significant cementitious calcium silicate hydrated phases from characterization, fabrication of nanocomposite cementitious materials, and finally application of cementitious materials as a component for capturing of toxic gases.

The objectives of this thesis are as follows:

- 1) Simulate eight important phases of calcium silicate and calcium silicate hydrated as our model systems at the microstructural levels within density functional theory (DFT) method.
- 2) Compute the bulk modulus of all eight phases according to Birth-Murnaghan equation of state.
- 3) Distinguish the wavenumber of $\nu(\text{Si-O})$ for all eight phases for four significant vibration modes.
- 4) Investigate the interaction mechanism of rGO surface moieties, such as hydroxyl (OH/rGO) and epoxide (Ep/rGO) groups with monomer of (calcium) silicate hydrates for various configurations to make composite cementitious materials.
- 5) Analyze the electronic properties of the ground-state structures obtained in the 4th objective through Bader charge analysis and density of state (DOS).
- 6) Determine the appropriate phase with the lowest surface energy to store carbon monoxide (CO), carbon dioxide (CO₂), nitric oxide (NO), and nitrogen dioxide (NO₂) gases within the nudged elastic band (NEB) through DFT calculation method and FTIR measurement.

Chapter 2

Correlation between Composition and Mechanical Properties of Calcium Silicate Hydrates Identified by Infrared Spectroscopy and Density Functional Theory

The results presented in this section of the thesis were obtained from my original work without involving other research groups. Reproduced with permission from [1]. Copyright 2019 American Chemical Society.

2.1 Characterization of Calcium Silicate Hydrate (CSH) and Calcium Silicate (CS) Phases

We have initially chosen eight various phases, which are identified as hydrated cement for our model systems, such as Tobermorite 14 Å [22, 78, 79], 11 Å [22, 80, 81], and 9 Å [22], Wollastonite [16, 22, 28, 31, 82], Jaffeite [22, 83], Jennite [22, 84, 85], γ -C₂S [22], and α -C₂SH [22, 86, 87].

Table 2.1: Characterization of Calcium silicate hydrate (CSH) and calcium silicate (CS) phases.
Reprinted from Ref. [1] with permission of The Journal of Physical Chemistry C.

Chemical name	Formula	C/S ratio	H/C ratio	Number of water molecules
Tobermorite 14	$\text{Ca}_8\text{Si}_{12}\text{O}_{47}\text{H}_{28}$	0.67	3.5	7
Tobermorite 11	$\text{Ca}_8\text{Si}_{12}\text{O}_{43}\text{H}_{20}$	0.67	2.5	5
Tobermorite 9	$\text{Ca}_8\text{Si}_{12}\text{O}_{33}\text{H}_2$	0.67	0.25	-
Wollastonite	CaSiO_3	1	-	-
Jennite	$\text{Ca}_9\text{Si}_6\text{O}_{32}\text{H}_{22}$	1.5	2.44	-
$\alpha\text{-C}_2\text{SH}$	$\text{Ca}_2\text{SiO}_5\text{H}_2$	2	1	-
$\gamma\text{-C}_2\text{S}$	Ca_2SiO_4	2	-	-
Jaffeite	$\text{Ca}_6\text{Si}_2\text{O}_{13}\text{H}_6$	3	1	-

Composition of calcium silicate (CS) and calcium silicate hydrate (CSH) phases are shown in table 2.1. Figure 2.1 illustrates the optimized unit cell side of tobermorite 14, 11, and 9 Å containing 7, 5, and 0 interlayer water molecules, respectively. Figure 2.2 shows wollastonite and jennite structures.

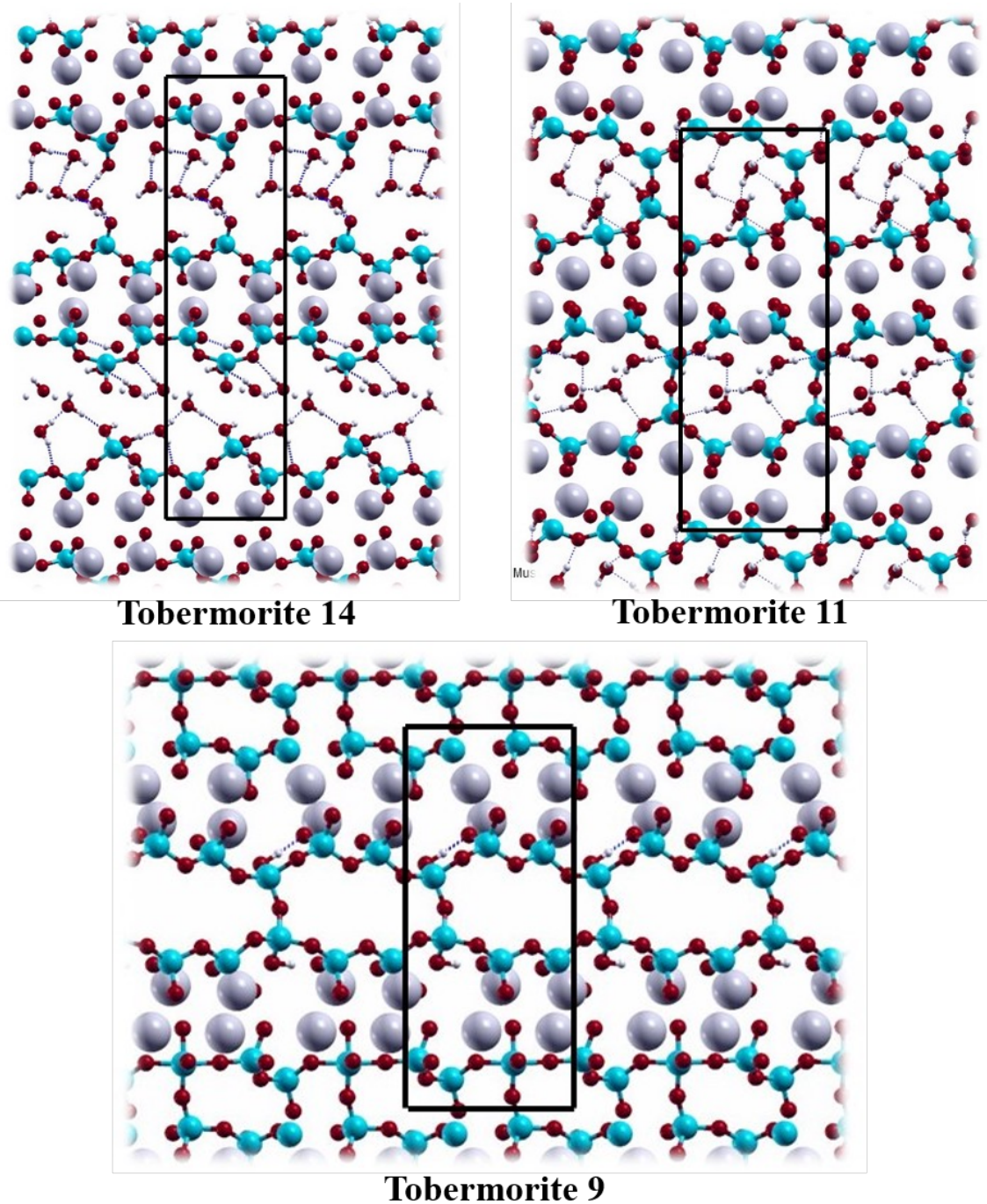


Figure 2.1: The unit cells of tobermorite 14, 11, 9 Å relaxed within DFT calculation. Modified with permission from [1]. Copyright (2019) The Journal of Physical Chemistry C.

It is also worth mentioning that tobermorite 14, 11, 9 Å, wollastonite and jennite structures illustrate 4-fold coordinated silicon tetrahedral chain. In contrast, the monomer structure of (CS) and (CSH), such as γ -C₂S, α -C₂SH, and jaffeite phases are also shown in Figure 2.3. Thus, tobermorite 14 Å can be taken into account as one of the major hydrated phase among them

due to 7 interlayer water molecule. On the other hand, γ -C₂S with silicate tetrahedra monomer structure is considered as the less hydrated phase containing no water molecule and hydroxyl groups.

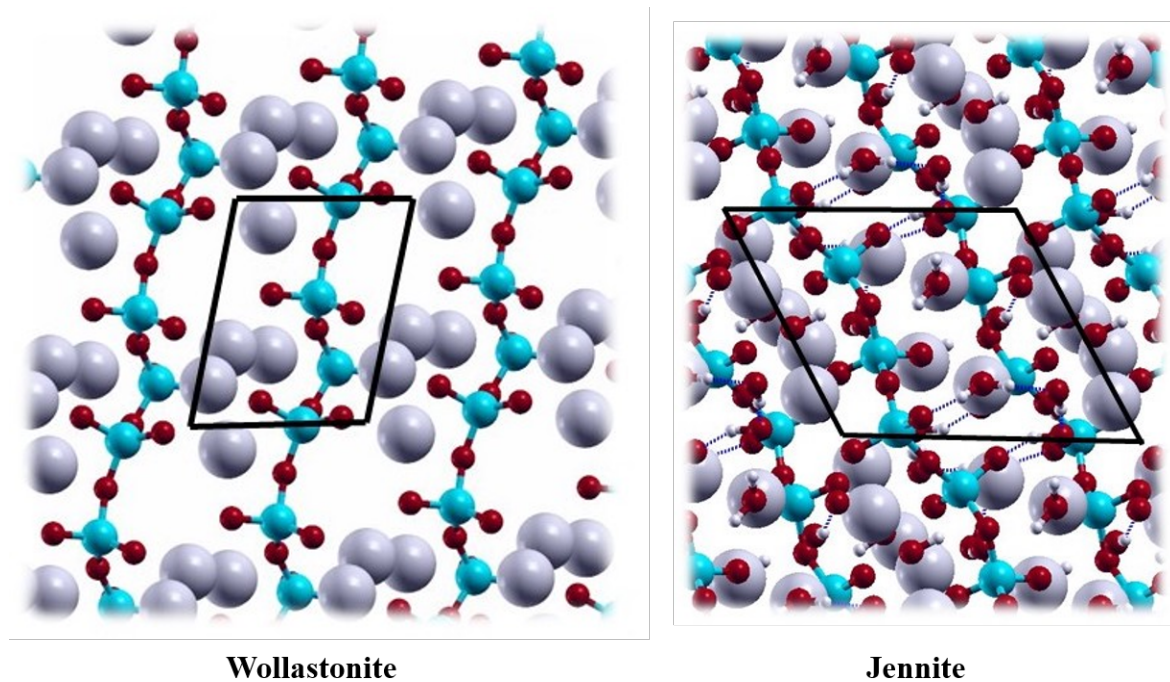


Figure 2.2: The unit cells of wollastonite, and jennite relaxed within DFT calculation. Modified with permission from [1]. Copyright (2019) The Journal of Physical Chemistry C.

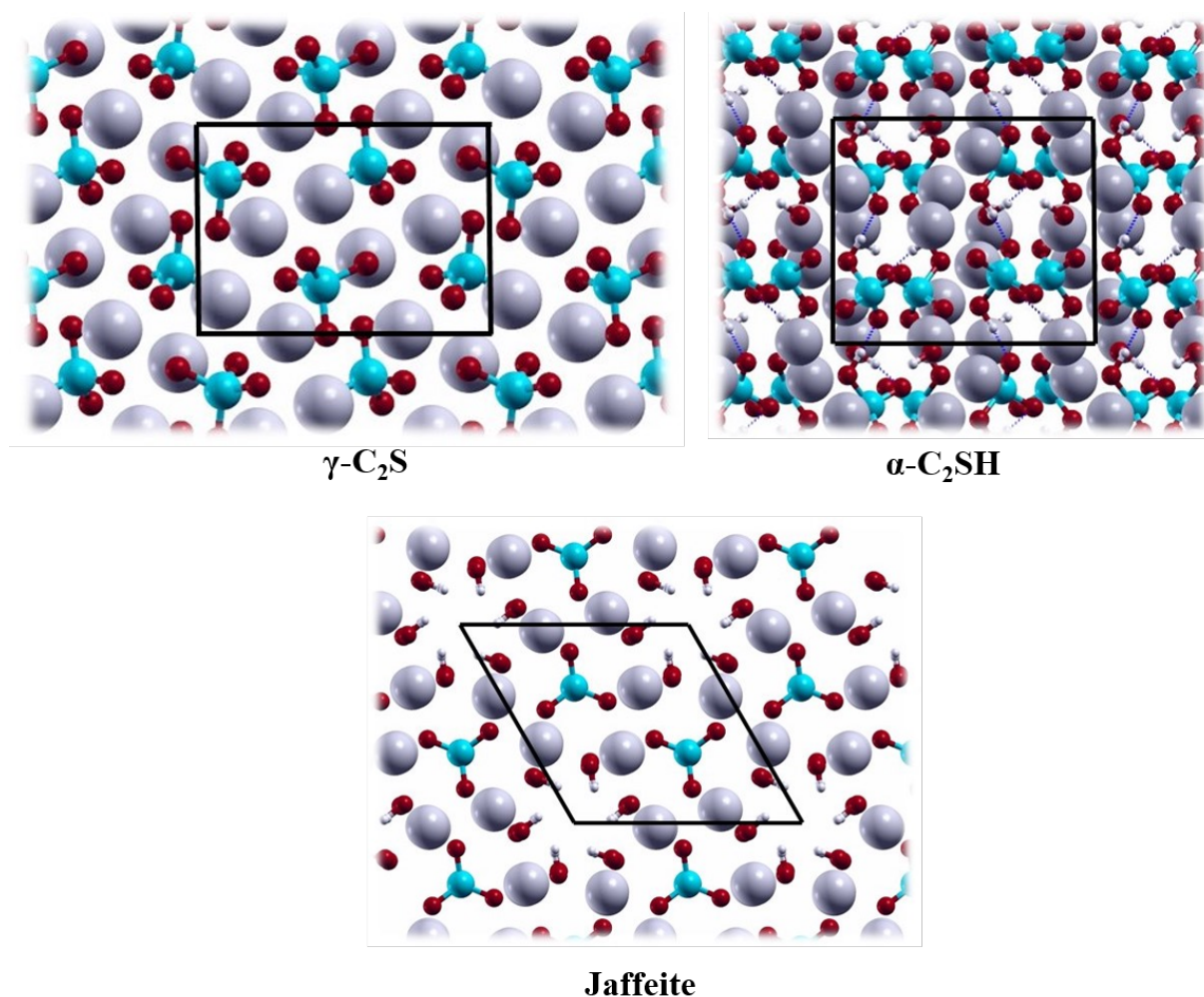


Figure 2.3: The unit cells of $\gamma\text{-C}_2\text{S}$, $\alpha\text{-C}_2\text{SH}$, and jaffeite relaxed within DFT calculation. Modified with permission from [1]. Copyright (2019) The Journal of Physical Chemistry C.

2.2 Calculations of Pressure and Bulk Modulus

In order to compute ten total energies of each phase, we have reduced the dimensions of each unit cell in all directions smaller or greater. Then, the E - V curve for each phase was plotted by connecting the calculated total energies, which indeed matches the equation of state from Birch-Murnaghan sketched in reference [88]. The diagrams of P - V were then calculated for all phases to evaluate the behavior of bulk modules, as illustrated in Figure 2.4a.

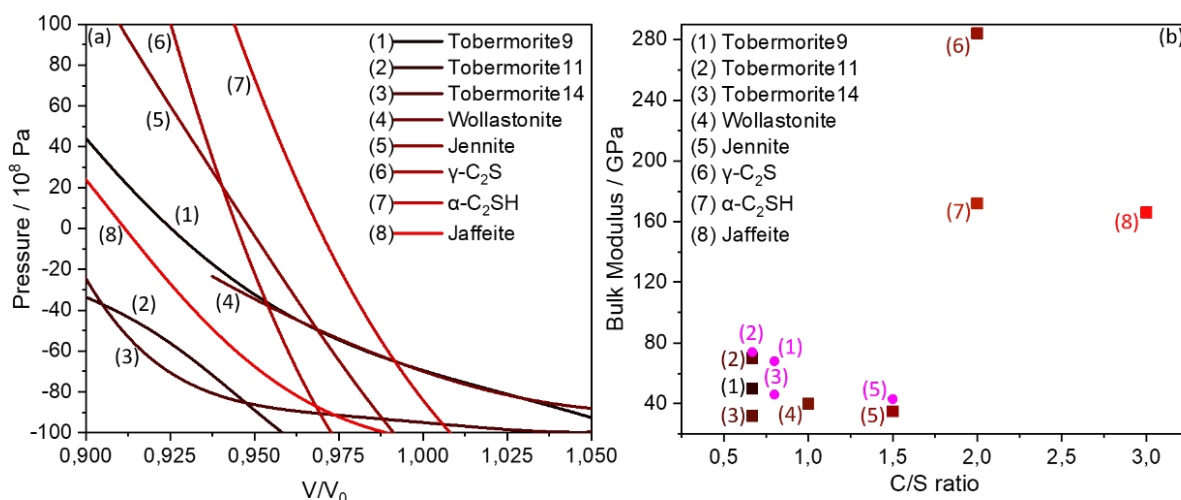


Figure 2.4: (a) Delta pressure of (CSH) and (CS) phases computed within DFT calculation. (b) In comparison to the rest of phases, γ -C₂S, α -C₂SH, and Jaffeite, represent a linear combination of bulk modulus. γ -C₂S and tobermorite 14 Å have the highest and lowest bulk modulus, respectively. Reprinted with permission from [1]. Copyright (2019) The Journal of Physical Chemistry C.

The horizontal axis indicates coefficients in the 0.9–1.1 ranges that have been employed to change the relaxed unit cell volumes of (CSH) and (CS) phases. Therefore, V_n and V were defined as the unit cell volume at the stationary point and the initial relaxed unit cell volume for each matching coefficient according to the Birch-Murnaghan equation of state, respectively. It was found that γ -C₂S, α -C₂SH, and Jaffeite phases behave like the isotropic solids as the slope of the diagrams were shown liner (Figure 2.4a). Due to the silicate tetrahedral monomer structure, γ -C₂S, α -C₂SH, and Jaffeite were considered as the utmost isotropic phases. The silicate tetrahedra monomer structure illustrates 4-fold coordinated silicon without formation of a silicate chain by binding to the neighboring silicate. In order to measure how the phases are resistant to the compression, the function of C/S ratio was considered. In fact, the presence of water placed into the structure of each phase was established as one of the primary parameters. Within DFT method, we measured the bulk modulus of all presented phases in this study. Equation 2 shows that the bulk modulus (K) can be computed by the following formula:

$$K = -V_0 \left[\frac{\Delta P}{(V_n - V_0)} \right]$$

The initial volume and volume at the stationary point of the unit cell are defined by V_0 and V_n , respectively. The change of pressure is also defined by ΔP .

Figure 2.4b shows the bulk modulus trends concerning all considered phases for this study. The bulk modulus for tobermorite 14, 11, 9 Å and jaffeite phases have been earlier measured by Manzano et al. [89] as were illustrated by the pink dots in Figure 2.4b. They reported the

bulk modulus of 46 and 68 GPa for tobermorite 14 and 9 Å as C/S ratio of them is identical and equivalent to 0.8, respectively. As stated earlier, the C/S ratio is dependent to the bulk modulus, and consequently the bulk modulus increases as the C/S ratio increases. Therefore, the results revealed by Manzano et al. confirmed that the bulk modulus of tobermorite 14 and 9 Å (C/S ratio of 0.8) raised by 43 and 36% compared to our results with the C/S ratio of 0.67, respectively. The bulk modulus concerning to jennite and tobermorite 11 Å were reported to be similar with our results.

2.3 Phases Development Process During the Hydration of Cement

The IR spectra of synthetic (CSH) has recently been studied. Walker et al. measured the FTIR measurement of samples having different C/S ratios ranging from 0.4 to 2. They prepared (CSH) gel, stored for period of 112 weeks at room temperature. Then, FTIR measurement has been performed for the samples. Then, all samples were then equilibrated for duration of 448 days. Walker et al. [90] reported on samples preparation that steady state obtained after 448 days. In fact, it is not true and the chemical reaction was prevented because the samples have been prepared by pressing into KBr pallets at a sample ratio of 1 mg to 100 mg of KBr. Though wavenumbers altered somewhat between 400 and 800 cm^{-1} for various C/S ratios from 0.4 to 2, it was not reported what kind of phases and fundamental vibration modes were recognized. Moreover, no shifting was detected for the wavenumbers between 3400 and 3800 cm^{-1} , and several new peaks emerged for C/S ratios of 1.7, 1.8, and 2. The material has, in other words, converted and new phases have been produced. Figure 2.5a indicates a primary model for phase of (CS) as a substantial cement phase afore exposure to water. The incomplete formation of (CSH) and (CS) phases were illustrated in Figure 2.5b including jennite, $\gamma\text{-C}_2\text{S}$, $\alpha\text{-C}_2\text{SH}$, and jaffeite after duration of 12 hours and afore complete hydration time. In fact, by time goes on, the number of phases enhances. Finally, the most important phases of tobermorite 14 (1), 11 (2), 9 Å (3), wollastonite (4), jennite (5), $\gamma\text{-C}_2\text{S}$ (6), $\alpha\text{-C}_2\text{SH}$ (7), and jaffeite (8) after complete process of hydration are plotted in Figure 2.5c.

Hydrated phases is dependent on the time and the number of them increases. Generally, correlation of peaks measured by FTIT spectra with specified vibration modes at the atomic scale is considered as one of the main concern of building materials.

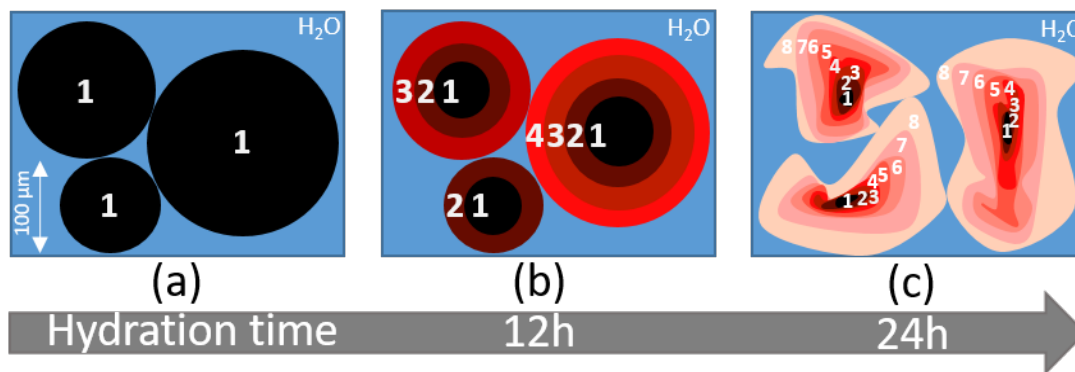


Figure 2.5: Time-dependent model consists of three levels for the phase fabrication process during the cement hydration. (a) Model of (CS) phase as the main initial cement structure afore interaction with water. (b) Phases formation slowly and gradually. (c) At the end, more pores emerge between phases and the form of all phases are changed. Reprinted with permission from [1]. Copyright (2019) The Journal of Physical Chemistry C.

2.4 IR Spectra of Calcium Silicate Hydrate (CSH) and Calcium Silicate (CS) Phases

The measured IR spectra of (CSH) and (CS) phases are illustrated in Figure 2.6. Based on the atomic data, the presence or even vibration mode shift can be discussed, for instance, as a function of the C/S and H/C ratios. Certainly, by increasing the C/S ratio, decrements are observed in the wavenumber, and consequently they are shifted. Figure 2.7 illustrates four significant vibration modes recognized for all of eight phases.

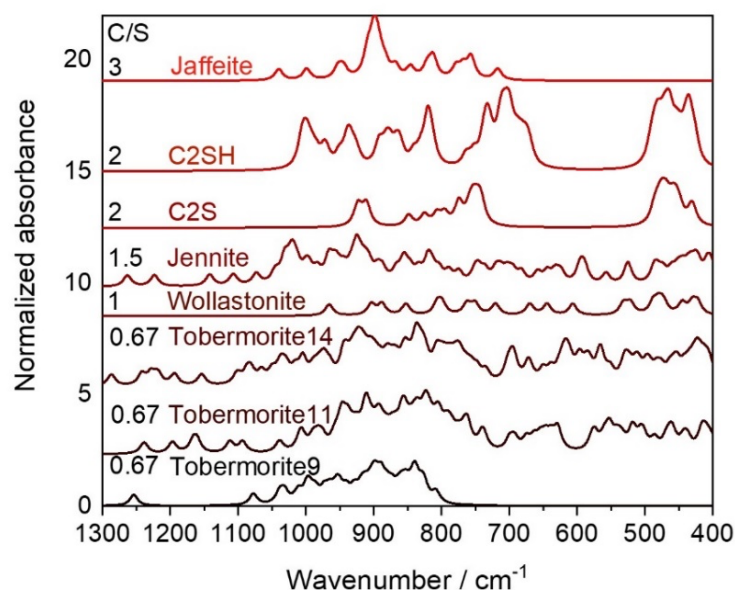


Figure 2.6: The selected calcium silicate hydrate (CSH) and calcium silicate (CS) phases as model systems for measurement of IR spectra. Reprinted with permission from [1]. Copyright (2019) The Journal of Physical Chemistry C.

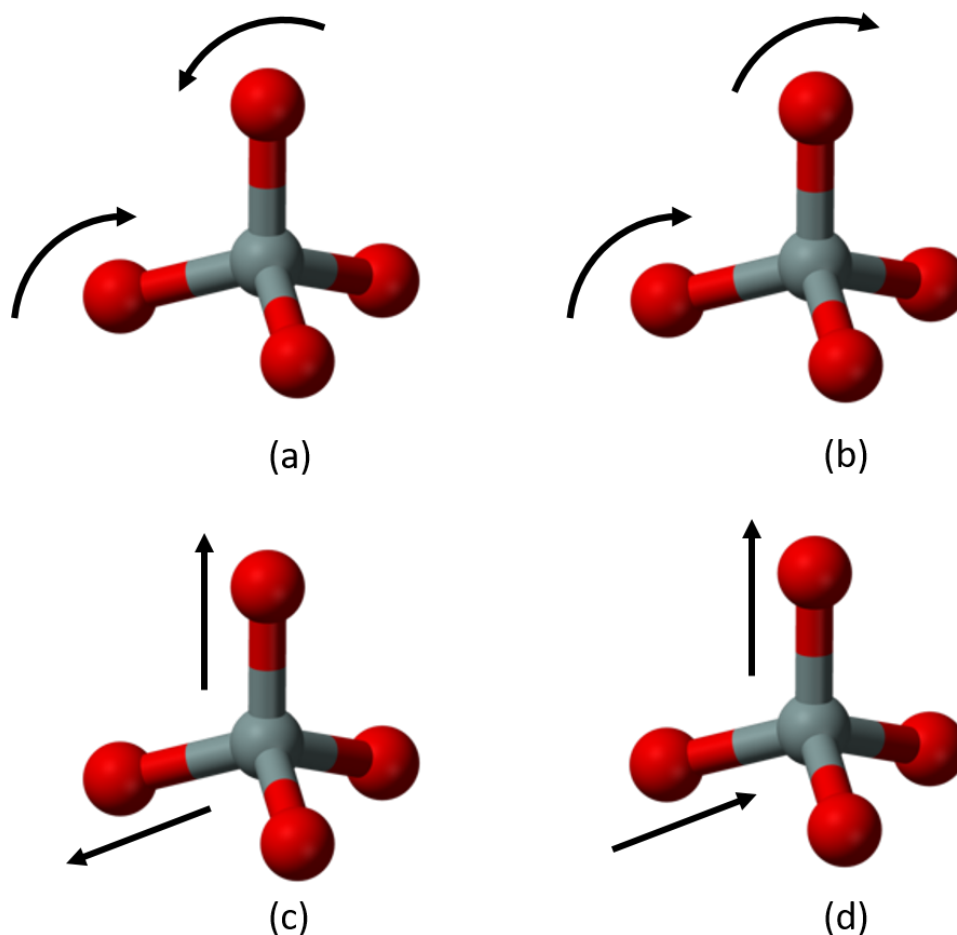


Figure 2.7: The application of four significant vibration modes to distinguish the wavenumber for silicon bonded to the oxygen $\nu(\text{Si-O})$ in silicate tetrahedra monomer structure and chains of silicate tetrahedra. (a,b) Deformation for symmetrical and asymmetrical modes, respectively. (c,d) Stretching for symmetrical and asymmetrical modes, respectively. Modified with permission from [1]. Copyright (2019) The Journal of Physical Chemistry C.

The wavenumber for silicon bonded to the oxygen $\nu(\text{Si-O})$ in the silicate tetrahedra monomer structure and chains of silicate tetrahedra as a function of various C/S and H/C ratios for four significant vibration modes are shown in Figure 2.8. The wavenumber for silicon bonded to the oxygen $\nu(\text{Si-O})$ in the silicate tetrahedra monomer structure and chains of silicate tetrahedra for four major vibration modes were found, which influenced by two major factors, such as presence of calcium atoms and hydrogen bonding. As a consequence, the computed wavenumber for silicon bonded to the oxygen $\nu(\text{Si-O})$ categorized and depicted as a function of the C/S and H/C ratios. In fact, a global trend was not revealed (Figure 2.8) for the wavenumber for silicon bonded to the oxygen $\nu(\text{Si-O})$ in the silicate tetrahedra monomer structure and chains of silicate tetrahedra for all vibration modes but recommended trends are dependent on the constant C/S or H/C ratio.

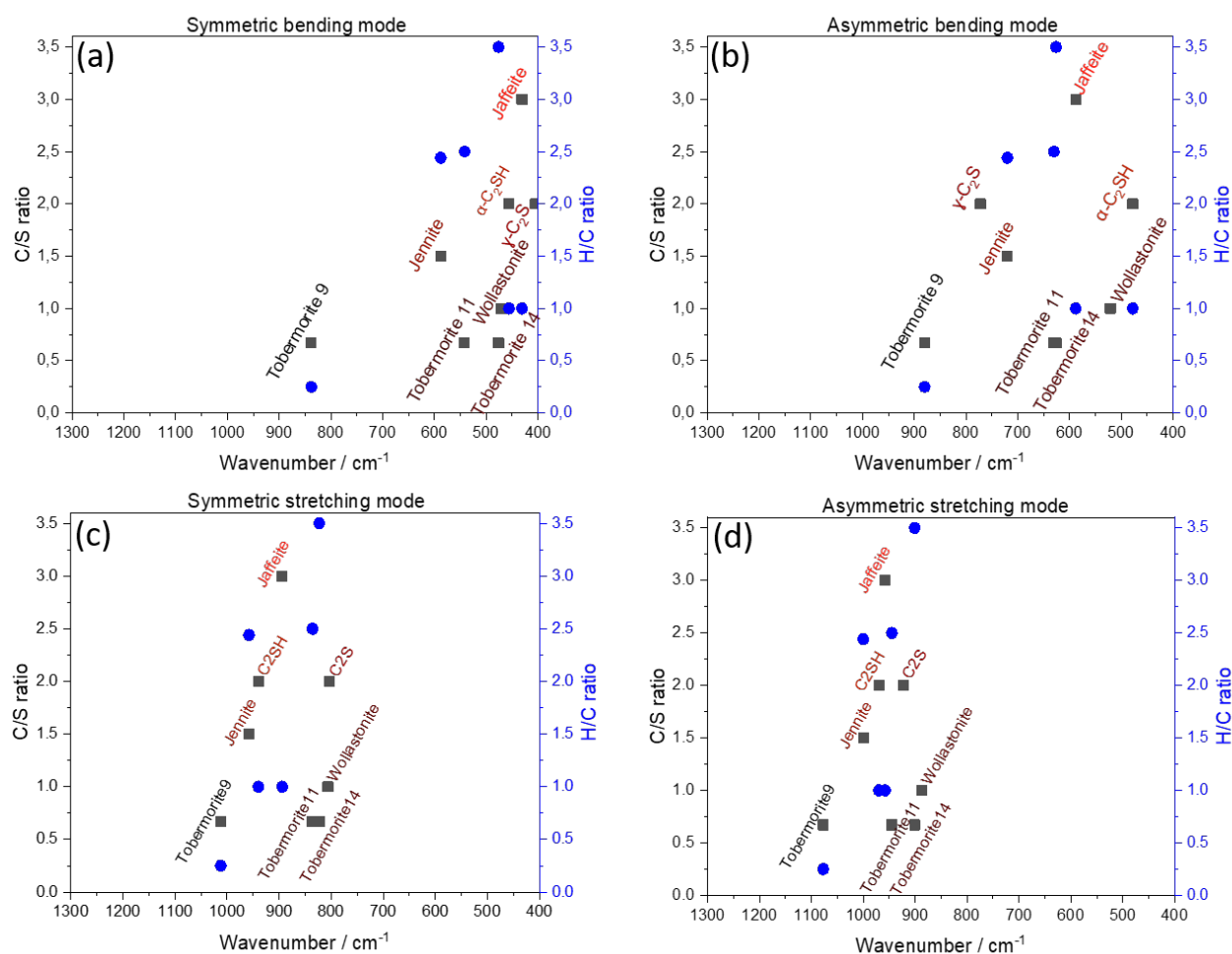


Figure 2.8: The wavenumbers for silicon bonded to the oxygen $\nu(\text{Si-O})$ for four significant vibration modes in the silicate tetrahedra monomer structure and chains of silicate tetrahedra. (a,b) The wavenumbers for symmetrical and asymmetrical bending modes as a function of various C/S and H/C ratios. (c,d) The wavenumbers for symmetrical and asymmetrical stretching modes as a function of various C/S and H/C ratios. Reprinted with permission from [1]. Copyright (2019) The Journal of Physical Chemistry C.

Initially, it has been found that when as H/C ratios increase for the identical C/S ratio, the wavenumbers of silicon bonded to the oxygen $\nu(\text{Si-O})$ decrease as well. For instance, with the identical C/S ratios for tobermorite 9, 11 and 14 Å, the wavenumbers of $\nu(\text{Si-O})$ from tobermorite 14 to 9 Å increase because the H/C ratios decrease. Moreover, the contribution of the C/S ratio at roughly similar H/C ratio for tobermorite 11 Å in comparison with jennite. tobermorite 11 Å represents a lower wavenumber of $\nu(\text{Si-O})$ than jennite due to the lower C/S ratio.

2.5 Summary

DFT modeling method was used to simulate and relax the eight significant phases of (CSH) and (CS) structures, such as tobermorite 14, 11, 9 Å, wollastonite, jaffeite, jennite, γ -C₂S, and α -C₂SH, which are developed through the hydration process of cement as our model systems. Accordant with the Birch–Murnaghan equation of state, E - V curve for each phase was plotted to compute the bulk modulus. According to the calculation of the bulk modulus of all phases, the highest and lowest bulk modulus were obtained for γ -C₂S and tobermorite 14 Å, respectively. On the one hand, the most isotropic phases were found in α -C₂SH, γ -C₂S, and jaffeite due to the silicate tetrahedra monomer structure. One of the major issue of construction materials was to find a correlation between the single peaks obtained in FTIR measurement with specified vibration modes at the atomistic scale. We thus used the optimized structures of all phases in order to determine the wavenumber for silicon bonded to the oxygen $\nu(\text{Si-O})$ within DFT calculation depending on the two different criteria of C/S and H/C ratios in the silicate tetrahedra monomer structure and chains of silicate tetrahedra for four major vibration modes. Although a global trend was not found in the wavenumber of $\nu(\text{Si-O})$ for (CS) and (CSH) phases, two theories based on the constant C/S or H/C ratio can be followed. The wavenumbers of $\nu(\text{Si-O})$ have a tendency to decrease for the constant C/S ratio as H/C ratios increase. On the contrary, the wavenumbers of $\nu(\text{Si-O})$ increase for the identical H/C ratio as C/S ratios increase. Therefore, it has been observed that jennite represents a higher wavenumber for silicon bonded to oxygen $\nu(\text{Si-O})$ than tobermorite 11 Å due to the higher C/S ratio.

Chapter 3

Interaction of Reduced Graphene Oxide with Monomers of (Calcium) Silicate Hydrates: A First-Principles Study

The results presented in this section of the thesis were obtained from my original work in collaboration with Dr. Dolado and Dr. Ayuela from Materials Physics Center (CFM) institute as Karlsruhe House of Young Science (KHYS) financed me to expand my research study abroad.

3.1 Hydroxyl/rGO with Silicate Hydrate Moieties

3.1.1 Hydroxyl/rGO with the $\text{Si}(\text{OH})_4$ silicate hydrate unit

In order to explore the binding effect of rGO surface moieties with calcium silicate hydrate units for fabrication of cementitious nanocomposite material, we have initially examined the interaction mechanism of $\text{Si}(\text{OH})_4$ hydrated silicate monomer with hydroxyl/rGO as the starting point. Therefore, two diverse configurations have been prepared for our simulation models, which $\text{Si}(\text{OH})_4$ was situated in two various positions from hydroxyl/rGO sheet as the starting geometric structures. Our observations demonstrated that for the ground-state structure, the water molecule, pure graphene, and $\text{SiO}(\text{OH})_3$ (Figure 3.1b) are the final productions with the lower ground-state energy when $\text{Si}(\text{OH})_4$ is deposited a bit farther from the hydroxyl/rGO sheet as the starting geometric structure. We also observed a lower ground-state energy of 0.289 eV for the ground-state structure containing $\text{SiO}(\text{OH})_3$, water molecule and pure graphene plane

(Figure 3.1b) in comparison with the other optimized configuration (Figure 3.1a), which the starting geometry was not changed after optimization.

We also computed the adsorption energies of $\text{SiO}(\text{OH})_3$ and $\text{Si}(\text{OH})_4$. According to the former studies, Wu et al.[91] investigated that the adsorption energy of L-leucine on the graphene sheet is from -0.17 to -0.31 eV for the different of L-leucine/graphene configurations. Guo [92] also studied that the adsorption energy of arginine-glycine-aspartic acid (RGD) on graphene sheet, which is about -1.206 eV. In the present study, the adsorption energies of $\text{SiO}(\text{OH})_3$ and $\text{Si}(\text{OH})_4$ have been computed, which are -1.683 eV and -0.094 eV, respectively. Thus, $\text{SiO}(\text{OH})_3$ at the ground-state structure has the lower adsorption energy of 1.589 eV in comparison to the other configuration, which demonstrates that the system containing $\text{SiO}(\text{OH})_3$ with water and pure graphene plane as the most stable configuration.

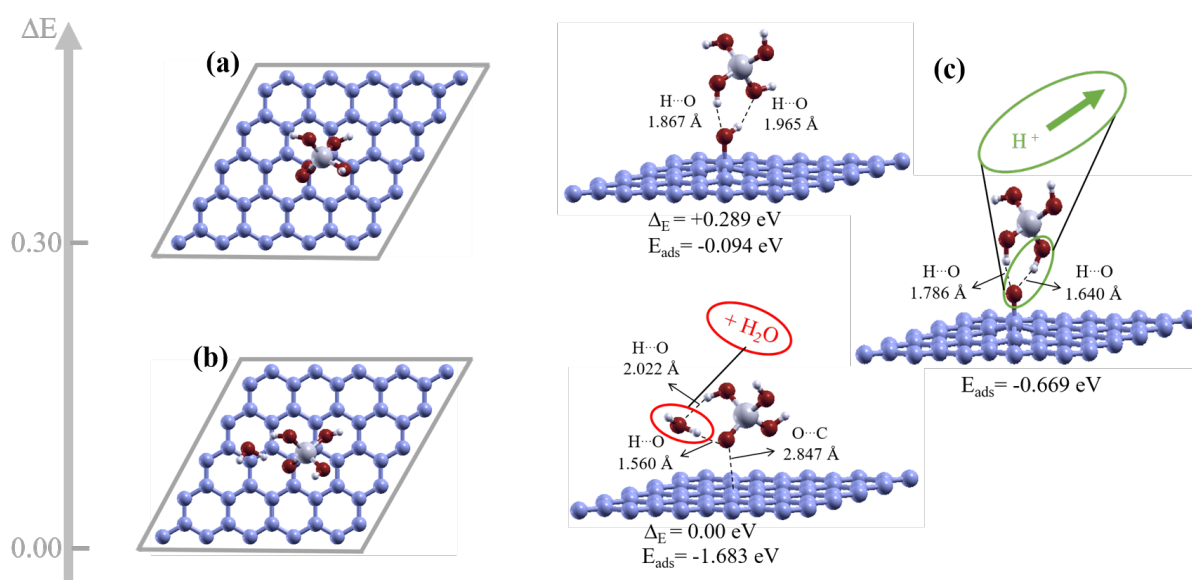


Figure 3.1: Top view and side views of geometric configurations obtained from the initial geometric structure of $\text{Si}(\text{OH})_4$ on hydroxyl/rGO sheet. (a) Expected optimized physisorbed configuration, and (b) ground-state obtained as an optimized geometric structure including a water molecule and a $\text{SiO}(\text{OH})_3$ unit on the graphene plane. (c) Optimized geometric structure obtained from $\text{SiO}(\text{OH})_3$ on the hydroxyl/rGO sheets for singly-negative charged systems. The energy difference ΔE and the adsorption energies of $\text{Si}(\text{OH})_4$ or $\text{SiO}(\text{OH})_3$ are also indicated below each configuration.

On the one hand, the interaction mechanism of $\text{SiO}(\text{OH})_3$ unit on the hydroxyl/rGO was studied for the singly-negative charged system. It was surprisingly found that the hydrogen was dissociated from hydroxyl/rGO plane and went to the $\text{SiO}(\text{OH})_3$ unit to saturate the dangling oxygen as was illustrated in Figure 3.1c. It is also worth mentioning that we deposited $\text{SiO}(\text{OH})_3$

on the hydroxyl/rGO for the neutral system as the initial simulation model as well, and likewise we observed that the hydrogen was dissociated from hydroxyl/rGO surface and travels to the $\text{SiO}(\text{OH})_3$ unit. Irrespective of neutral or charged systems, a dissociation of hydrogen from hydroxyl/rGO surface is carried out. Thus, a dangling oxygen points to the graphene plane and is nearly full occupied by the charge transfer from the graphene sheet.

3.1.2 Graphene with H_2O and $\text{SiO}(\text{OH})_3$ for four different configurations

After thorough examination for two different configurations of $\text{Si}(\text{OH})_4$ respect to the distance with hydroxyl/rGO sheet, we distinguished that the optimized geometric structures consisting of $\text{SiO}(\text{OH})_3$, water molecule and graphene as the ground-state structure and the most stable configuration (Figure 3.1b). Thus, in this part of investigation, we look into four various configurations to specify the best location of water molecule as the ground-state structure. The ground-state structure has been portrayed in Figure 3.2.a because of two reasons. First, water molecule is located near to the graphene surface for more interaction with it. Second, two strong O-H bonds (shorter length) with $\text{SiO}(\text{OH})_3$. For the ground-state structure as shown in Figure 3a, the lower energies of 0.087, 0.215, and 0.2847 eV have been obtained in comparison to the rest of configurations as indicated in Figures 3.2(b-d), respectively. In fact, the various configurations for H_2O led to the various adsorption energies, which the adsorption energies of $\text{SiO}(\text{OH})_3$ for ground-state structure and the rest of configurations are equivalent to -1.683, -1.596, -1.468 and -1.436 eV.

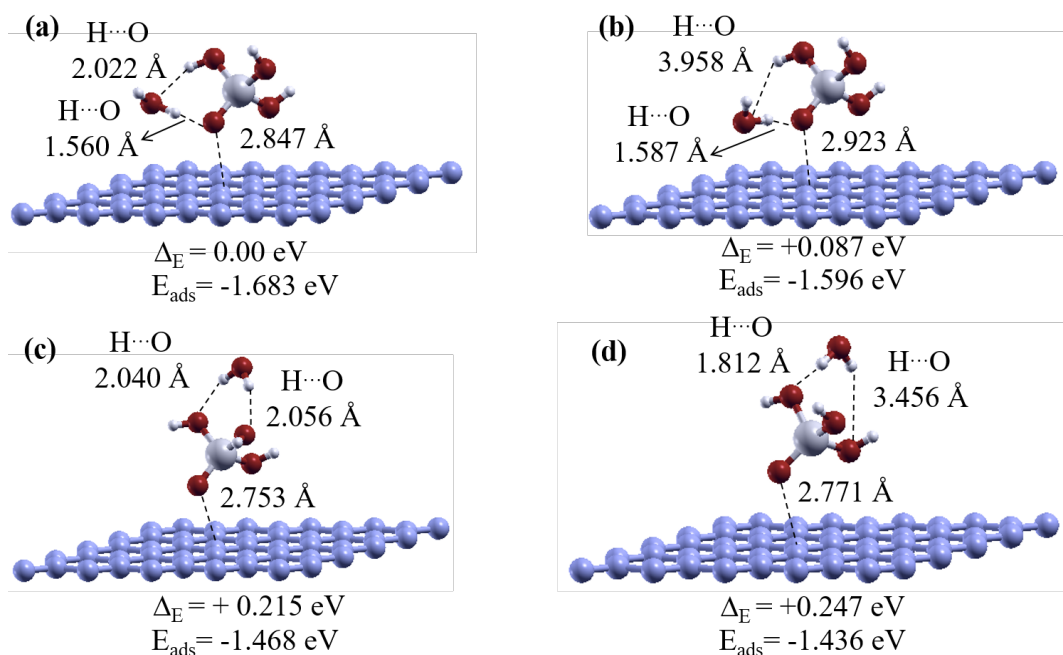


Figure 3.2: (a-d) display the optimized geometric structures including water molecule and SiO(OH)_3 on the graphene plane for four different configurations of water molecule positions as the initial geometric structures.

3.1.3 Computational models of SiO(OH)_3 units on the graphene plane: chemisorbed and physisorbed configurations

To a further understanding of the adsorption properties of SiO(OH)_3 for the neutral and singly-negative charged systems on graphene surface, we have deposited them on the graphene plane respect to diverse distances for four various configurations. The ground-state structures for the neutral and singly-negative charged systems correlated with the physisorbed unit of SiO(OH)_3 on the graphene plane. The optimized and ground-state structures for the systems of neutral and singly-negative charged are shown in Figure 3.3. From grey curve can be observed that SiO(OH)_3 contributed with physisorbed on the graphene plane for the ground-state structure with a lower energy state of 0.23 eV in comparison with a chemisorbed configuration. For the singly-negative charged system, both optimized and ground-state structures show the physisorbed interaction of SiO(OH)_3 on the graphene plane. Wu. et al. [91] found that *L*-leucine molecule for both perpendicular and parallel adsorption models to the graphene surface, the low E_B was clearly connected with physisorption. Fan et al. [93] has moreover shown that graphene layer is mainly physically adsorbed on the surface for both O-polar and Si-polar surfaces.

The adsorption energies of $\text{SiO}(\text{OH})_3$ for two different configurations in the neutral system were calculated and it was found that the ground-state structure has lower energy of 0.230 eV in comparison with other configuration (gray curve in Figure 3.3). In contrast, the adsorption energies of 2.164 and 2.216 eV for $\text{SiO}(\text{OH})_3^-$ for two identical physisorbed configurations in singly-negative charged system were computed (pink curve in Figure 3.3). Since the adsorption energy must be negative, it is worth to clarify the reason for positive values of adsorption energies by ground-state energy computation. We computed the ground-state energies of $\text{SiO}(\text{OH})_3$ and $\text{SiO}(\text{OH})_3^-$ equal to -45.195 and -50.350 eV, respectively. The ground-state energies of $\text{SiO}(\text{OH})_3$ or $\text{SiO}(\text{OH})_3^-$ with graphene plane equal to -507.833 and -509.236 eV, respectively. Although, the ground-state energy difference between $\text{SiO}(\text{OH})_3$ and $\text{SiO}(\text{OH})_3^-$ is -5.155 eV and it was expected after deposition of $\text{SiO}(\text{OH})_3$ on the graphene sheet for the neutral and singly-negative charged system, the almost identical ground-state energy difference of -5.155 eV was obtained, the ground-state energy difference of -1.403 eV was calculated. The reason can be explained that in the configuration consist of $\text{SiO}(\text{OH})_3$ and graphene, charge transfer was performed from graphene sheet to 2p orbital of dangling oxygen atom in $\text{SiO}(\text{OH})_3$ to compensate the lack of electron and make it almost full occupied, regardless of adding one further electron to the system. Nonetheless, after adding an extra electron to the system in order to make the system as a neutral, a big portion of an extra electron goes to the graphene sheet and the ground-state energy of the whole system was somewhat decreased not as much as we expected (decreased -1.403 eV instead of -5.155 eV), thereby the positive adsorption energy for the $\text{SiO}(\text{OH})_3^-$ was computed.

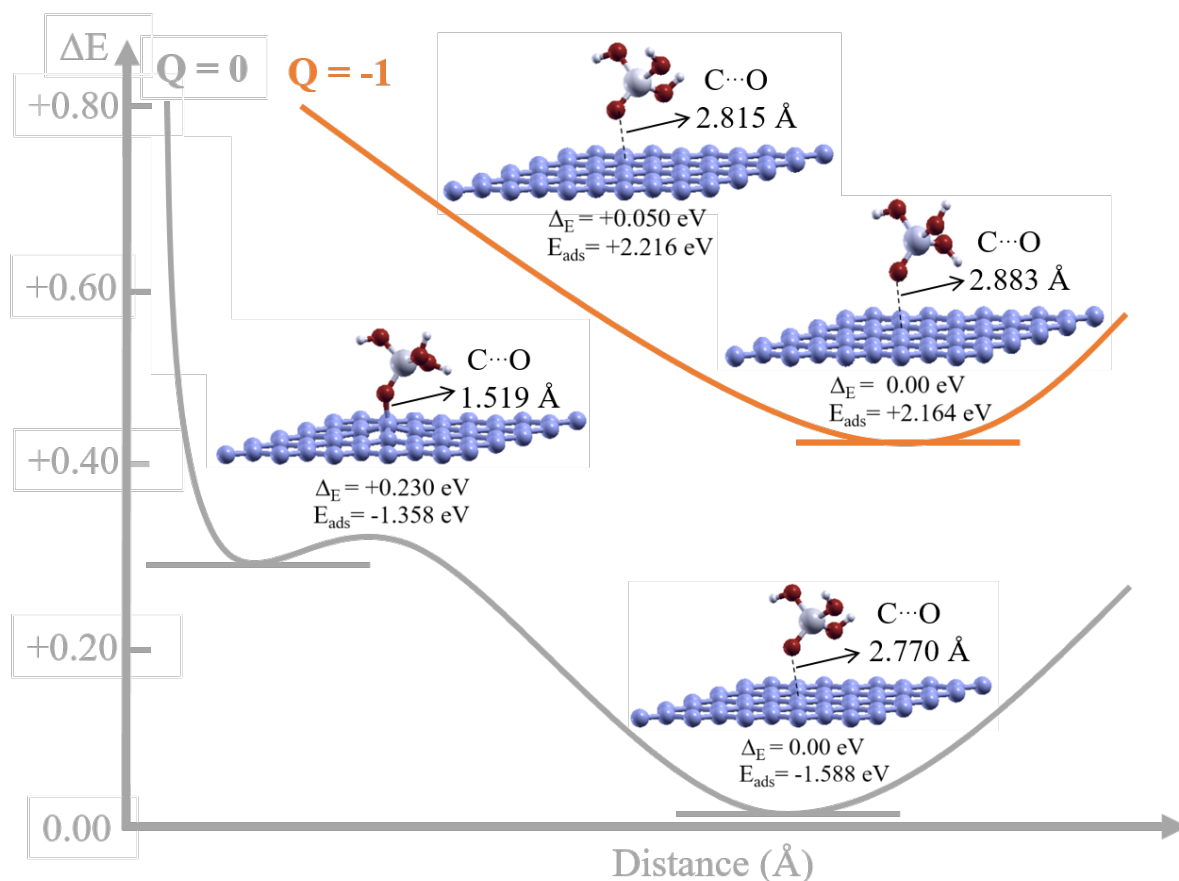


Figure 3.3: Energy scheme of the relaxed geometric structures involving $\text{SiO}(\text{OH})_3$ units on graphene. We found two initial different chemisorbed and physisorbed configurations as a function of the distance between the graphene plane and $\text{SiO}(\text{OH})_3$ for the neutral systems and for singly-negative charged system it becomes physisorbed configurations. The energy difference ΔE (in eVs) of each configuration was given below for each charge state. The adsorption energies with respect to $\text{SiO}(\text{OH})_3$ units are included also below the configurations.

3.2 Hydroxyl/rGO Combined with Calcium Silicate Hydrate Units in the Presence of Ca and Hydroxyl Groups

3.2.1 Hydroxyl/rGO with silicate hydrate units, in the presence of Ca

In this part of study, we have investigated the interaction of $\text{Si}(\text{OH})_4$ on the hydroxyl/rGO sheet in the presence Ca (Figure 3.4a). In fact, two various configurations were prepared as the Ca were deposited close and far away from $\text{Si}(\text{OH})_4$ on the hydroxyl/rGO sheet as the initial geometry structures. When the optimized geometric structures achieved, the results show that the ground-state energy of the configuration with close deposited Ca (see Fig. 3.4a) found to be 0.495 eV lower than the other configuration with far way deposited Ca. In fact, the charge

transfer was performed from graphene sheet to 2p orbital of oxygen atom in $\text{SiO}(\text{OH})_3$ for the same configuration without Ca. Therefore, for the initial system including Ca, Ca is involved in the interaction with $\text{SiO}(\text{OH})_3$. The partial charge transformation takes place from Ca to 2p orbital of dangling oxygen from $\text{SiO}(\text{OH})_3$ to make it fully occupied and the rest of charges transfer to the graphene sheet. On the other hand, for doubly-positive charged system, the structure of $\text{Si}(\text{OH})_4$ on the substrate of hydroxyl/rGO was optimized in the presence of Ca. It has also been observed that the hydroxyl group dissociated from the substrate of hydroxyl/rGO resulting formation of water molecule and, moreover, Ca involved in the interaction with $\text{SiO}(\text{OH})_3$. It is concluded that even for doubly-positive charged system as a neutral system, the contribution of graphene sheet is more substantial because of that the electrons are discharged from graphene sheet. The distance between Ca to the dangling oxygen from $\text{SiO}(\text{OH})_3$ are 2.075 and 2.127 Å for the optimized structure of close and far away deposited Ca as the initial structure. Therefore, for the ground-state structure, the distance of Ca to the oxygen atom is 0.052 Å closer than other configuration.

Depending on four various configurations for water molecule on the graphene surface, the adsorption energies of $\text{SiO}(\text{OH})_3$ can be changing from -1.43 to -1.69 eV. Furthermore, the adsorption energies of $\text{SiO}(\text{OH})_3$ were computed to be from -1.36 to -1.59 eV in the absence of water molecule on the graphene surface for the neutral system (gray curve in Figure 3.3). Surprisingly, the adsorption of $\text{SiO}(\text{OH})_3$ decreased remarkably to be -4.382 or -6.22 eV, depending on the two different configurations in the presence of water molecule and Ca on the graphene surface (Figure 3.4a,b). In conclusion, the reduction of adsorption energy is attributed to a reason that the new system contains Ca.

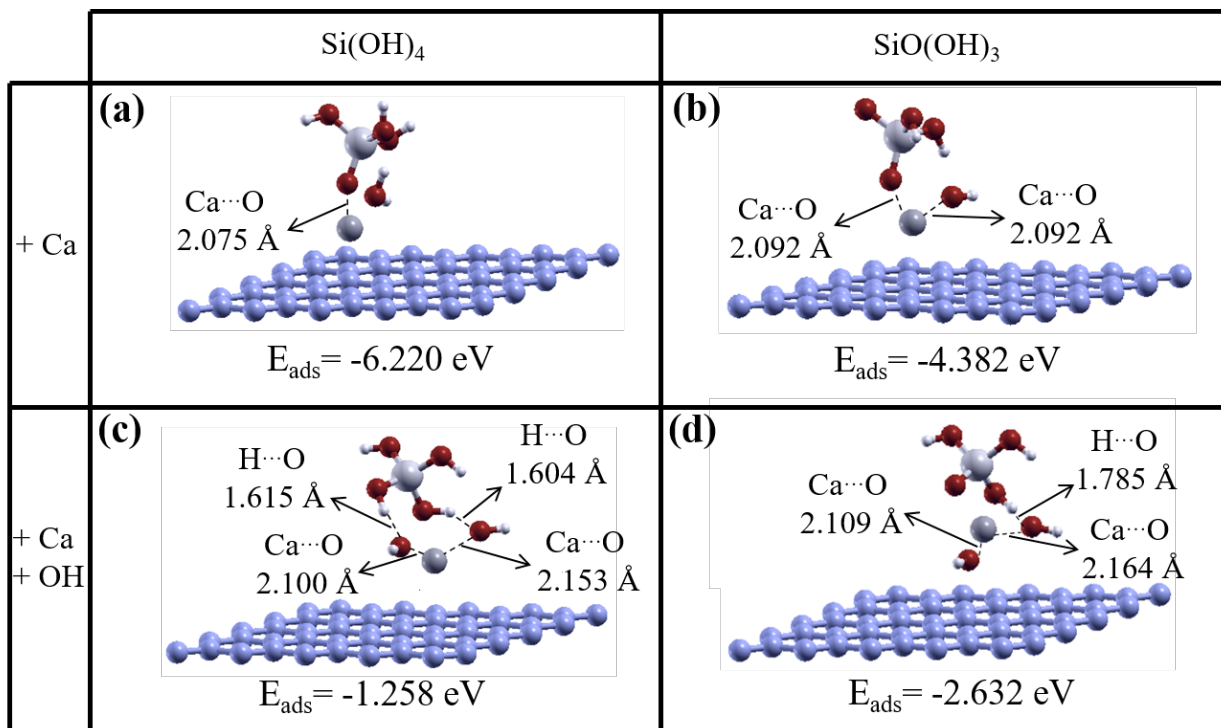


Figure 3.4: Optimized geometric structures including silicate hydrate units, Si(OH)₄ or SiO(OH)₃, and Ca on the graphene plane, when Ca were initially deposited close to the units on the hydroxyl/rGO sheet. Upper panels involve a Ca; below panels, a Ca and also hydroxyl groups. The adsorption energies of SiO(OH)₃ or Si(OH)₄ are also indicated below each configuration.

On the one hand, we have investigated the interaction of SiO(OH)₃ on the hydroxyl/rGO sheet in the presence Ca (Figure 3.4b). In fact, two various configurations were prepared as the Ca were deposited close and far away from SiO(OH)₃ on the hydroxyl/rGO sheet as the initial geometry structures. It must be mentioned that the hydroxyl group has not been dissociated from the hydroxyl/rGO sheet for the system that Ca has been deposited far away from SiO(OH)₃ as the initial simulation model. A lower energy of 1.932 eV has been computed for the ground-state structure obtained for the system that the Ca was deposited near to the SiO(OH)₃ on the hydroxyl/rGO sheet as the initial simulation model in comparison with far away deposited Ca. It is also worth reporting that for the ground-state structure, the dissociated hydroxyl group from hydroxyl/rGO can be involved in bonding with Ca. Therefore, the charge transformation can take place from Ca to two neighboring oxygen atoms from SiO(OH)₃ and dissociated hydroxyl group to make them entirely occupied (Figure 3.4b).

3.2.2 Hydroxyl/rGO with silicate hydrate units, in the presence of Ca involving a hydroxyl group

We moreover examined the interaction mechanism of Si(OH)_4 and SiO(OH)_3 on the hydroxyl/rGO sheet in the presence Ca with a hydroxyl group (Figure 3.4c,d). The ground-state structures were obtained for the configurations with close deposited Ca resulting dissociation of the hydroxyl group from hydroxyl/rGO sheets. Figure 3.4c,d indicates that Ca were involved into two neighboring oxygen atoms to transfer charges. The lower energies of 3 and 0.4 eV for the ground-state structures of Si(OH)_4 and SiO(OH)_3 were calculated in comparison with the other configurations, respectively. On the contrary, the hydroxyl groups from hydroxyl/rGO sheets were not dissociated for far away deposited Ca configuration. The lower adsorption energy of 3.588 eV obtained for SiO(OH)_3 in the system with condensation reaction in comparison with the system including Ca and hydroxyl group. By deposition of more hydroxyl group to the system, the hydroxyl group from hydroxyl/rGO sheet is dissociated as the hydroxyl groups from Si(OH)_4 are strongly bonded to Si atom.

3.3 Epoxide/rGO with Calcium Silicate Hydrate Units

In the section of 3.1.1, we demonstrated that dissociation of hydroxyl group from hydroxyl/rGO sheet resulting condensation reaction and production of pure graphene for the ground-state structure of Si(OH)_4 on the hydroxyl/rGO sheet (Figure 3.1b). In contrast, Figure 3.5a illustrates that the ground-state structure remains almost closely to the initial simulation model and pure graphene was not produced as Si(OH)_4 is deposited on epoxide/rGO surface. The interaction of SiO(OH)_3 on the epoxide/rGO sheet was also examined (Figure 3.5b). It was found that the lower adsorption energy 0.726 eV was computed for SiO(OH)_3 (Figure 3.5b) in comparison to Si(OH)_4 (Figure 3.5a) on the epoxide/rGO surface. It must be mentioned that the SiO(OH)_3 unit shifted away from the epoxide group due to physisorbed interaction with graphene sheet as discussed earlier. Finally, SiO(OH)_3 was deposited on epoxide/rGO sheet in the presence of two hydroxyl groups and Ca to make a neutral system, as shown in Figure 3.5c. As we discussed earlier in the section 3.2.1, the most favorable adsorption energy gains for a system including Ca; therefore, the adsorption energy of SiO(OH)_3 containing Ca and functional group of hydroxyl declined by 1.521 eV (Figure 3.5c) in comparison to the same structure but without Ca and functional groups (Figure 3.5b).

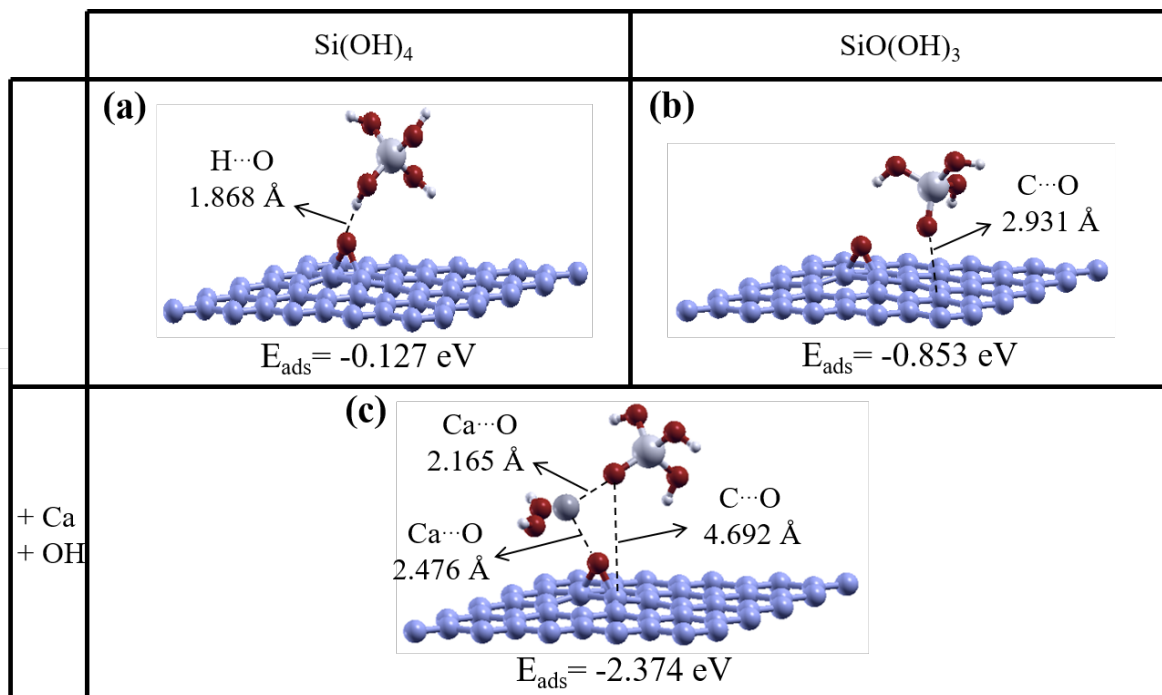


Figure 3.5: Optimized geometric structures of (calcium) silicate hydrate units on the epoxide/rGO sheet. The adsorption energies are also indicated below the geometrical configurations. Note that the adsorption of the units with epoxide/rGO becomes more favorable including Ca.

3.4 Discussions

3.4.1 Electronic properties of the ground-state structure with condensation reaction

In this part of investigations, the electronic properties of the ground-state structures have been detected above are analyzed in more details. The total DOS of the ground-state structure comprising of $\text{SiO}(\text{OH})_3$, graphene layer and water molecule units are shown in Figure 3.6a. The vertical dashed line, which set to the zero shows the fermi level value. The Fermi level located below the charge neutrality point of the graphene layer, being positively charged. The pink color curves illustrate the projected DOS of dangling oxygen atom belonging to $\text{SiO}(\text{OH})_3$. At the valance band energy of -0.073 eV as shown below the Fermi level, the large DOS illustrates a peak from the oxygen atom with almost more than one extra electron. Moreover, we employed Bader charge analysis to analyze the charge density distribution of atoms, as seen in Figure 3.6b. From dangling oxygen of $\text{SiO}(\text{OH})_3$ can be observed that the amount of electros at the valance band is almost fully occupied by charge transfer from graphene sheet. In order words, the total number of electrons at the valance band of all atoms in $\text{Si}(\text{OH})_3$ exceeded by 0.67 electrons due to the charge transformation from graphene sheet to $\text{SiO}(\text{OH})_3$ moiety.

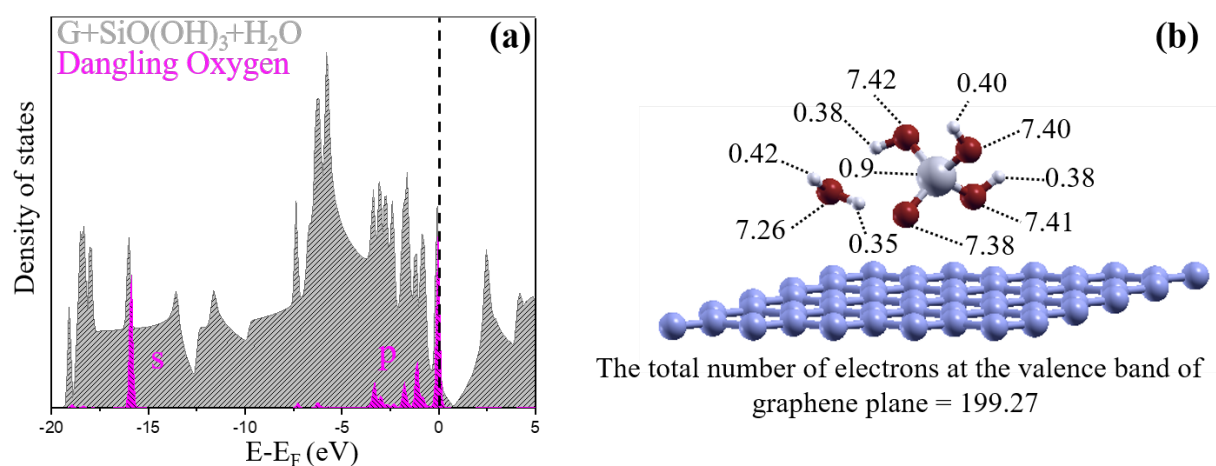


Figure 3.6: (a) Density of states and (b) charge distribution of the ground-state found for rGO with hydroxyl groups, which is compound of a water molecule and a $\text{SiO}(\text{OH})_3$ moiety on the graphene plane. The Fermi level is marked by dashed line and assigned to zero. The partial density of states on the dangling oxygen is also included using pink color. The charges are associated to atoms using Bader charge analysis.

3.4.2 Electronic properties of the ground-state $\text{SiO}(\text{OH})_3$ with graphene sheet

In this part of study, the ground-state structure of $\text{SiO}(\text{OH})_3$ on the graphene sheet for the neutral system was selected in order to study the electronic properties by Bader charge analysis method as illustrated in Figure 3.7a. As it is observed from Figure 3.7a, the graphene sheet lost 0.62 electrons and became 199.38 electrons and the total charge density of $\text{SiO}(\text{OH})_3$ at the valence bands became 31.62. In fact, the charge density of dangling oxygen at the valence band became almost fully occupied and equals to 7.32 electrons (Figure 3.7a). In order to display the distribution of charges between the substrate and absorbent, 3D charge density difference plot was constructed. Thus, Figure 3.7b illustrates the distribution of charge density difference for the neutral system of $\text{SiO}(\text{OH})_3$ on the graphene plane obtained as the ground-state structure, in respect of the $\text{SiO}(\text{OH})_3$ unit (31 electrons) and graphene sheet (200 electrons). Purple and yellow isosurfaces show charge loss and gain, respectively. Through Bader charge analysis, we have also evidenced that the electrons travel to the $\text{SiO}(\text{OH})_3$ unit from graphene sheet as illustrated by the number of electrons at the valence band of each atom. It can be explained that the charges transfer between $\text{SiO}(\text{OH})_3$ unit and graphene sheet to few Ås distance due to Coulomb interaction.

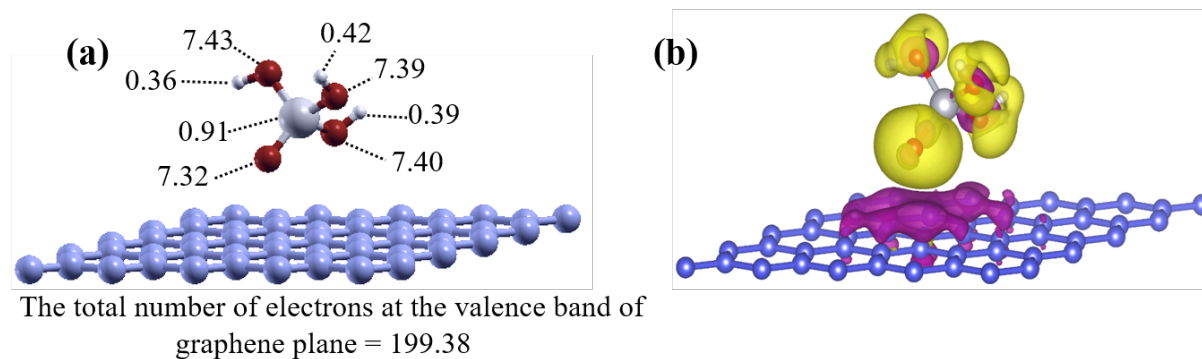


Figure 3.7: (a-b) Charge density distributions of the neutral model with the $\text{SiO}(\text{OH})_3$ unit physisorbed on graphene using Bader charge analysis and spatially 3D charge density differences. Yellow and purple isosurfaces indicate charge gain and loss, respectively. Note that nearly an electron goes to the $\text{SiO}(\text{OH})_3$ unit from the graphene layer to establish a strong bond which is stabilized further by the water molecule as shown by the adsorption energies.

3.4.3 Electronic properties of the ground-state with condensation reaction on the addition of Ca ion

In this part, the ground-state structure system consisting of $\text{SiO}(\text{OH})_3$ and water molecule in the presence of Ca on the graphene sheet was selected in order to study the electronic properties. In fact, among four various configurations (Figure 3.2), we have selected the system with the most favorable adsorption energy (Figure 3.2.a). Therefore, Figure 3.8 illustrates the DOS and Bader charge analysis for the most stable configuration. Based on the DOS analysis (Figure 3.8a), the charge neutrality point of the graphene layer is located below the Fermi level due to charge transfer from Ca to the graphene layer, being negatively charged. The calcium and dangling oxygen states, which are located away from the neutrality point in the graphene and Fermi level are showing roughly empty and fully occupied states, respectively. According to the Bader charge analysis (Figure 3.8b), it can be observed that dangling oxygen from $\text{SiO}(\text{OH})_3$ gets more charges in the presence of Ca than a system without Ca (Figure 3.6b). Through Bader charge analysis can also be observed that Ca became almost unoccupied with remaining charge of 0.42 electrons, and consequently the graphene sheet gains 0.82 electrons from Ca and became 200.82 electrons and the total charge density of $\text{SiO}(\text{OH})_3$ at the valence bands became 31.71. It seems that the Ca helps to make a sandwich structure between graphene layer and silicate hydrate unit with very favorable adsorption energies.

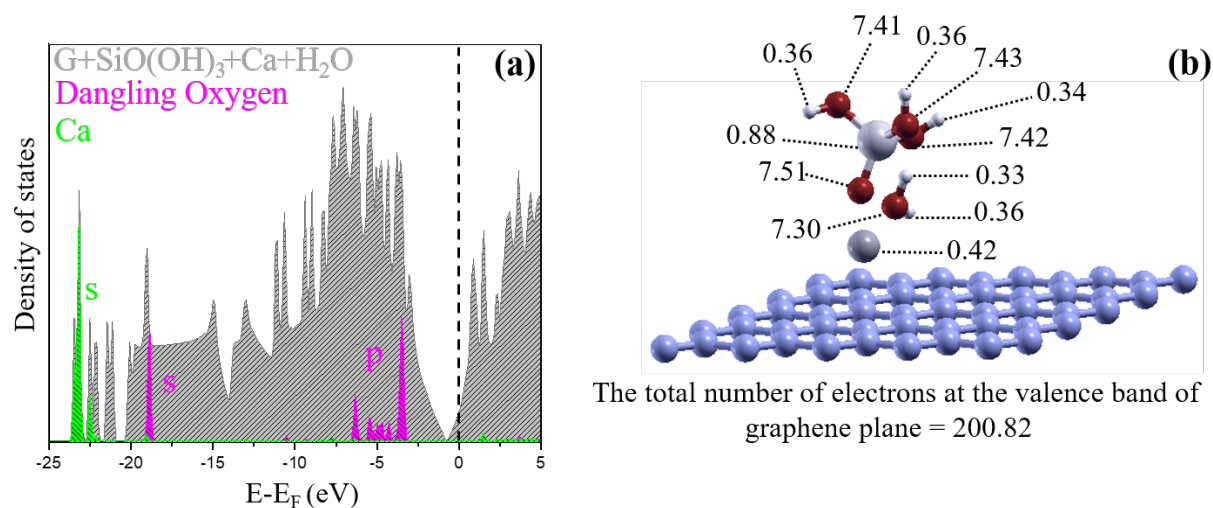


Figure 3.8: (a) Density of states and (b) charge distribution of the ground-state found for rGO with hydroxyl groups, which is compound of a water molecule, a $\text{SiO}(\text{OH})_3$ unit and a Ca ion on the graphene plane. The Fermi level is marked by dashed line and assigned to zero. The partial density of states on the dangling oxygen and calcium are also included using pink and green colors, respectively. The charges are associated to atoms using Bader charge analysis. Note that because of the Ca ion, the graphene layer is doped negatively. The dangling oxygen gets more charges and the silicate hydrate unit deposit over Ca ion on graphene.

3.4.4 Electronic properties of the ground-state epoxide/rGO with silicate hydrate unit

In Figure 3.9, we have finally shown the charge density distribution by Bader charge analysis and charge density difference of molecular orbital isosurfaces for the ground-state structure of epoxide/rGO with $\text{SiO}(\text{OH})_3$ in the case of neutral system. The total electrons of dangling oxygen are equivalent to 7.30, and therefore the total electrons of $\text{SiO}(\text{OH})_3$ unit became 31.55, as shown in Figure 3.9a. We also investigated the charge density distribution by adding one more electron into the system. Therefore, the density of dangling oxygen at the valence band somewhat increased from 7.30 to 7.46 electrons, 0.73 of electrons travels to the graphene plane, and 0.11 of electrons were shared by the rest of atoms. In order to display the distribution of charges between the substrate and absorbent, 3D charge density difference plot was constructed. Hence, Figure 3.9b demonstrates the distribution of electrons for the neutral system between substrate and absorbent according to Bader charge analysis. It was found that $\text{SiO}(\text{OH})_3$ unit was being negatively charged by the graphene plane as it was located far from the epoxide group. In fact, the bond between graphene and the $\text{SiO}(\text{OH})_3$ unit resembles the one given in the basic bonding model of that unit on graphene. At the end, from adsorption energies computation, we learnt that 2p orbital from dangling oxygen almost fully occupied by the charge transformation from graphene sheet to $\text{SiO}(\text{OH})_3$ for the neutral system.

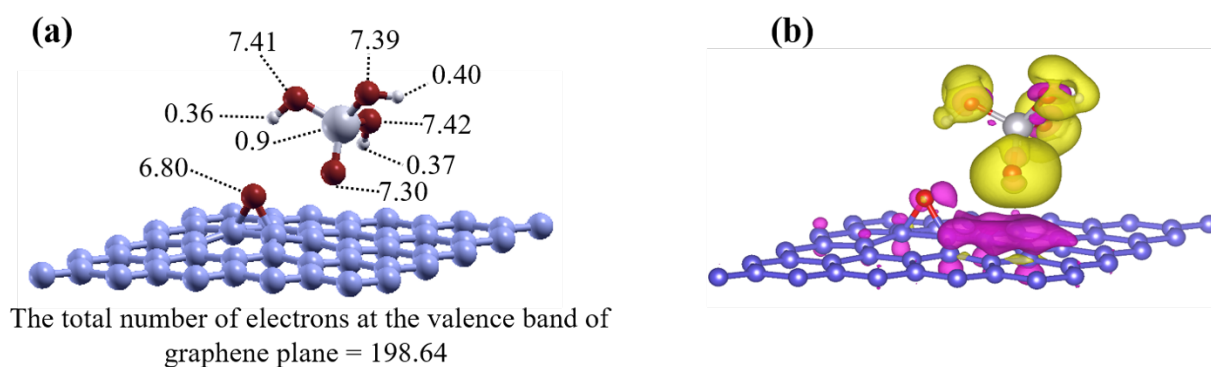


Figure 3.9: (a) Charge density distribution of $\text{SiO}(\text{OH})_3$ on the epoxide/rGO by Bader charge analysis. (b) 3D charge density difference for the neutral system. Yellow and purple isosurfaces indicate charge gain and loss, respectively.

3.5 Summary

By exfoliation and oxidation of graphite, reduced graphene oxide (rGO) sheet is produced and mainly coated by surface functional groups of hydroxyl and epoxide. Within DFT computational method, we employed reduced graphene oxide (rGO), which is highly occupied with hydroxyl and epoxide groups to study the interaction mechanism with calcium silicate hydrated (CSH) moieties for fabrication of nanocomposite materials. Therefore, we examined the interaction mechanism of reduced graphene oxide (rGO) coated by epoxide and hydroxyl groups with silicate hydrate units even in the presence of Ca and hydroxyl groups.

Initially, we found out that the interaction of hydroxyl/rGO with silicate tetrahedra can selectively repair the hydroxyl defects on the rGO lattice back into the graphene. Even in the presence of Ca, dissociation of defect from graphene sheet took place resulting condensation reaction. The Coulomb interaction was found as the main interaction between graphene plane and (CSH) gel because of charge transfer. In contrast, the ground-state structure obtained from the interaction mechanism of (CSH) gel with epoxide/rGO is almost identical with the initial structure model.

Moreover, we examined the electronic properties for some calculated ground-state structures by DOS and Bader charge analysis. We have also displayed the distribution of charges between the substrate and absorbent by 3D charge density difference plot. We found that the Fermi level was located below the charge neutrality point of the graphene layer, being positively charged in a system consisting of Si(OH)_3 , water and graphene sheet. On the contrary, for the same system with contribution of Ca, the Fermi level was located above the charge neutrality point of the graphene layer, being negatively charged.

Chapter 4

Capture of Toxic Gases by Cementitious Components

The computational results presented in this section of the thesis were obtained from my original work in collaboration with Dr. Natzeck for experimental results.

4.1 CO Deposition at the Surface of Tobermorite 11 Å (004)

The first part of this study exemplifies the CO deposition at the surface of tobermorite resulting formation of CO₃, which is absolutely dependent from the solid-state diffusion of the interlayer water of mineral. We on the one hand remind the readers that according to the former studies carried out in the UHV condition, CO can be adsorbed and make monolayer on the metal-clusters or minerals [94-97]. Initially, from experimental method, tobermorite powder was placed into the UHV condition to assure the dry surface. Different doses of carbon monoxide were then injected to the system at the surface of tobermorite. Surprisingly, we found a barrier-less chemical reaction of carbon monoxide with tobermorite resulting the interlayer water dissociation and formation of carbonates on the surface of tobermorite. Therefore, IR spectra of the adsorption of different dosing of CO molecule (10, 100, 1000, 10000 mL) on the surface of tobermorite 11 Å (004) is indicated in the Figure 4.1. In Figure 4.2, we have moreover displayed the absorbance for each particular wavenumber obtained from Figure 4.1, as a function of different CO dosing.

Figure 4.1a,b illustrate the significant peaks for the two stretching vibrations of $\nu(\text{C-O})$ and $\nu_{\text{as}}(\text{CO}_3)$ at 2162 and 1501 cm^{-1} , respectively [30, 98]. The growing of CO_3 on the surface of tobermorite 11 Å (004) at the vibration of 1501 cm^{-1} is shown by an incremental trend for peak intensity as the injection of CO increases from 10 to 1000 mL. By 10000 mL of CO dosing, the grows of CO_3 slows down due to sufficient accumulation of CO_3 on the surface of tobermorite and the peak of CO appears at 2162 cm^{-1} for the CO molecule adsorption.

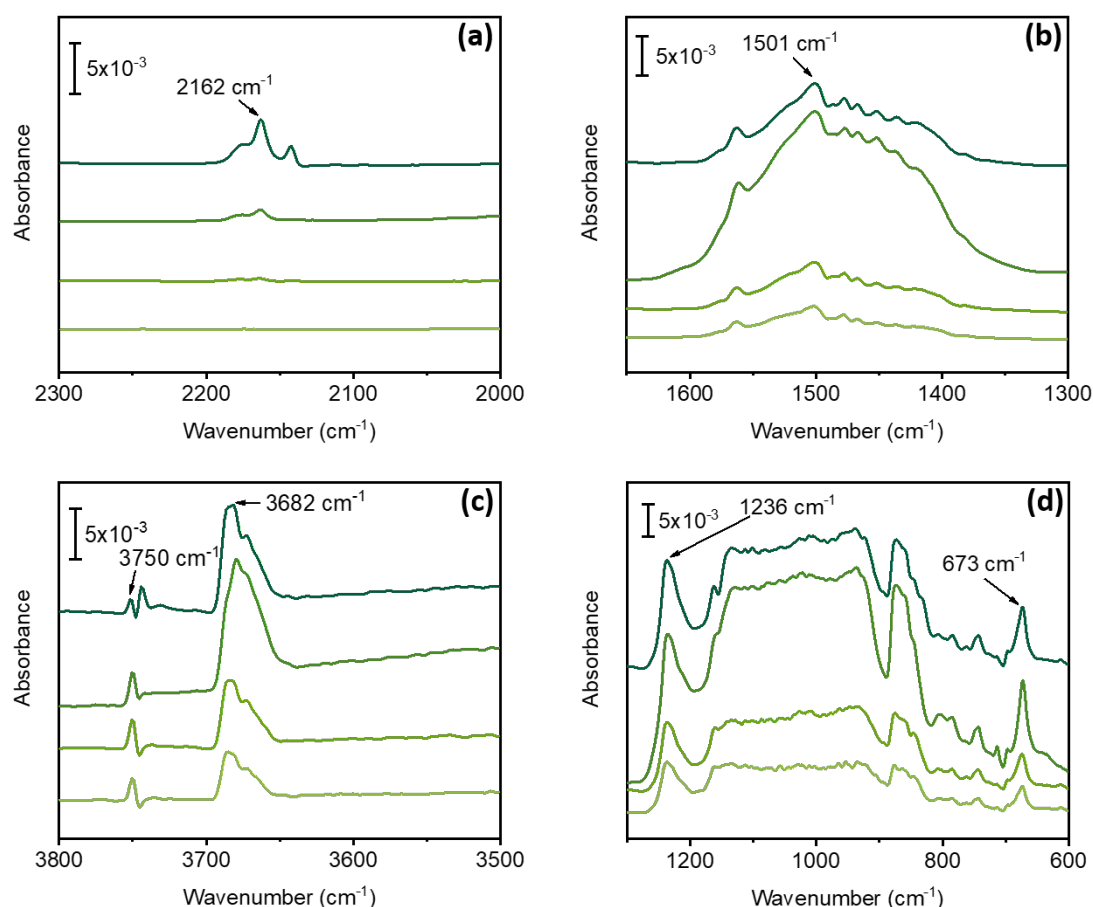


Figure 4.1: IR spectra of the adsorption of different dosing of CO molecule into the surface of tobermorite 11 Å (004). (a-d) indicate the classified IR spectrum including 2300-2000, 1650-1300, 3800-3500, and 1300-600, respectively. Light to dark green colors for the IR spectra represent the different dosing of CO (10, 100, 1000, 10000 mL), respectively.

In Figure 4.1c,d, together with the sequential dissociation of water molecule, the peaks intensities referring to the stretching vibrations of $\nu(\text{Ca-OH})$ and $\nu(\text{Si-OH})$ at 3682 and 3750 cm^{-1} were being ascended by increasing the dosing of CO from 10 to 1000 mL, respectively [30]. In contrast, by 10000 mL of CO dosing, the interlayer water molecules were not dissociated resulting a decreasing trend at the absorbance of Ca-OH and Si-OH comparing to 1000 mL, and consequently, the further growing of CO_3 on the surface of tobermorite were

stopped. The peaks corresponding to the bending and stretching vibrations of $\delta(\text{O-Si-O})$, $\nu(\text{Si-O})$ were seen at 673 and 1236 cm^{-1} , respectively [98].

To authenticate our results with the interlayer water-free mineral to observe the CO_3 formation at the surface, Thissen et al. [30] performed a study of CO at the mineral surface of wollastonite (001) with interlayer water-free and dry surface. As we expected, it was shown that the solid-state diffusion at the surface of wollastonite (001) with CO were not took place as the peaks of $\nu_{\text{as}}(\text{CO}_3)$, $\nu(\text{Ca-OH})$ and $\nu(\text{Si-OH})$ have not been observed in Figure 4.3 by UHV-FTIR measurement.

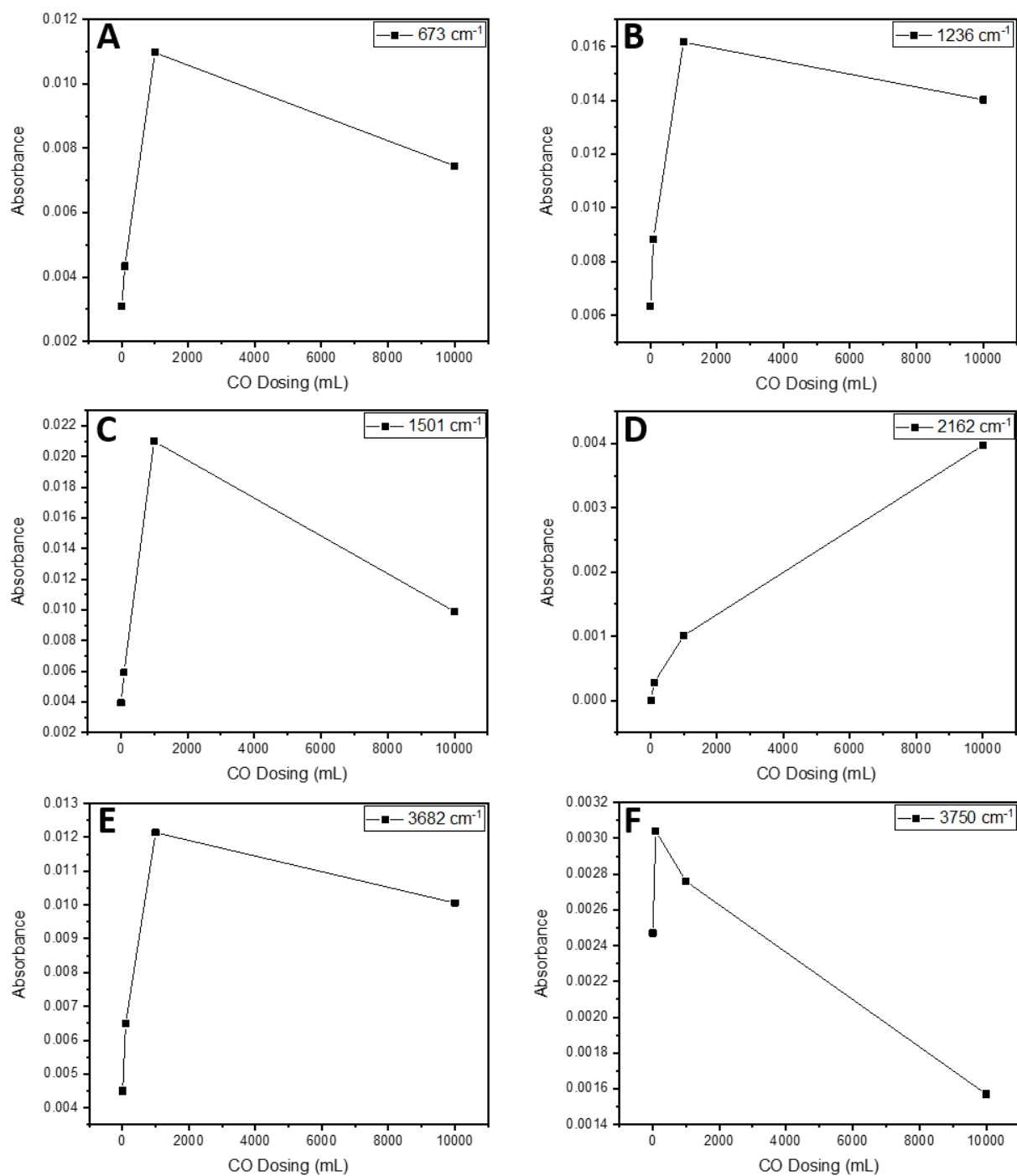


Figure 4.2: The absorbance for each particular wavenumber studied in Figure 4.1 as a function of different CO dosing.

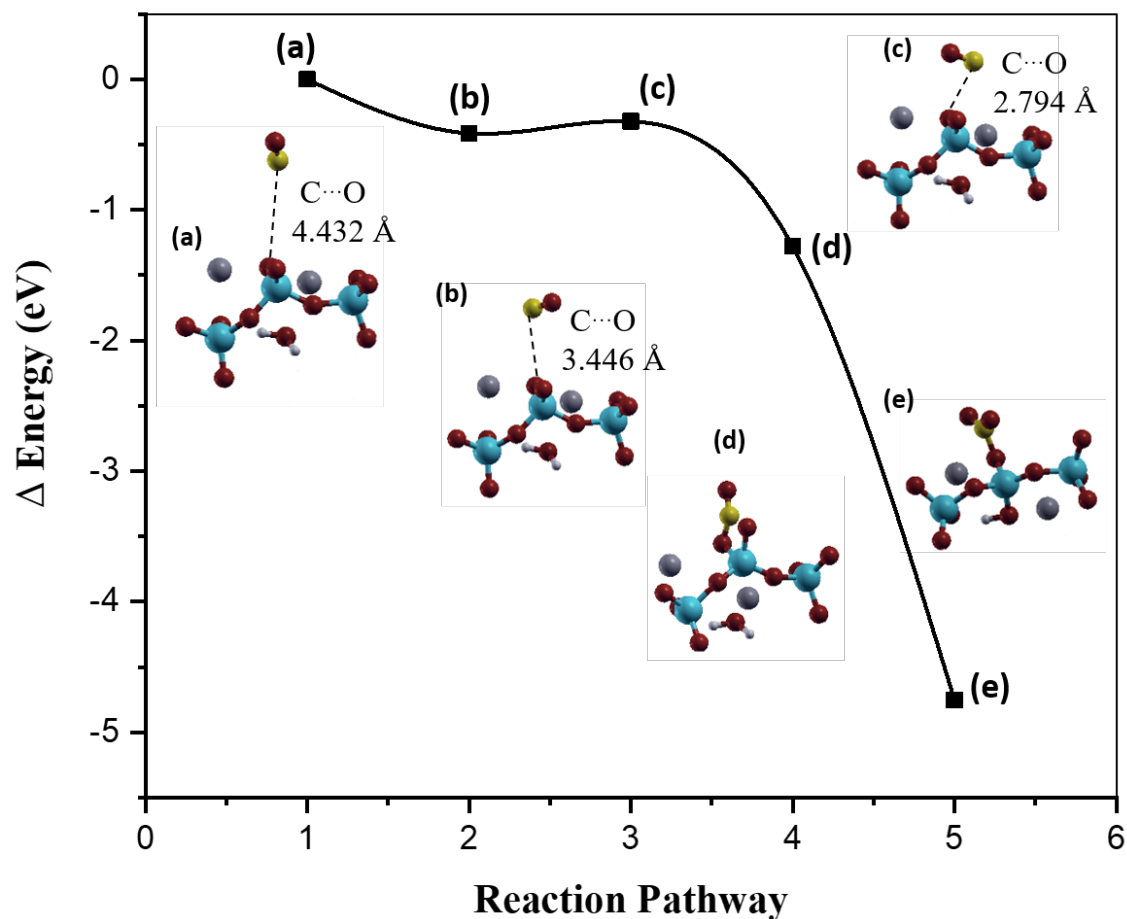
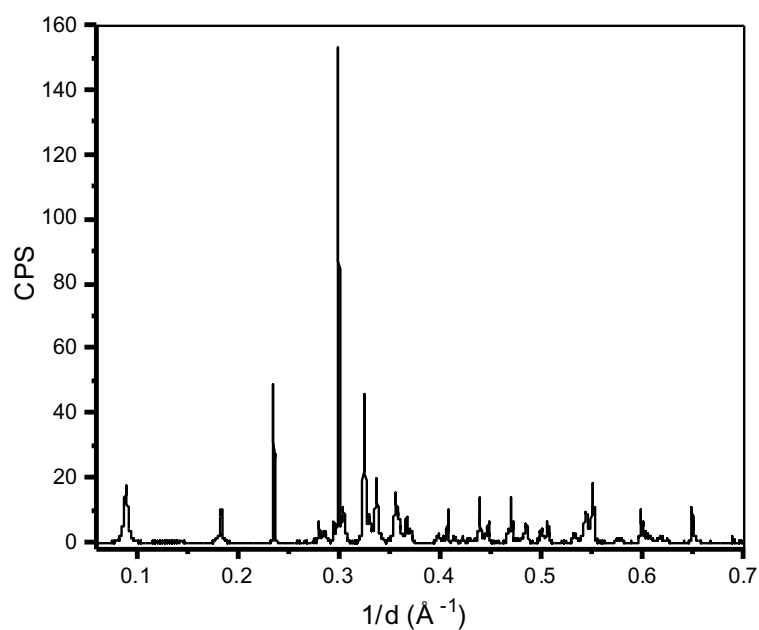


Figure 4.3: The DFT calculation of the barrier-less minimum energy path of CO reacting with the tobermorite 11 Å (004) resulting CO₃ formation at the surface and dissociation of interlayer water resulting solid-state diffusion. The light blue atoms represent Si; red, O; gray, Ca; white, H; yellow, C atoms, respectively.

To confirm our experimental results, we extend this study in the second part by computational validation of the first principles calculation to derive the possible mechanism. To simulate the appropriate phase among three different available tobermorite 9, 11 and 14 Å for the DFT calculation, X-ray Diffraction (XRD) analytical technique was exerted on the fresh sample of tobermorite powder. For detailed information, see the Figure 4.4 and accordingly can be seen that the majority of measured tobermorite is from type of 11 Å. In the following, to determine the proper surface for the tobermorite 11 Å with the carbon monoxide, the surface orientation of (004) with the lowest surface energy 0.41 J/m² (Table 1) selected as was reported by M. Mutisya [77].

(a)



(b)

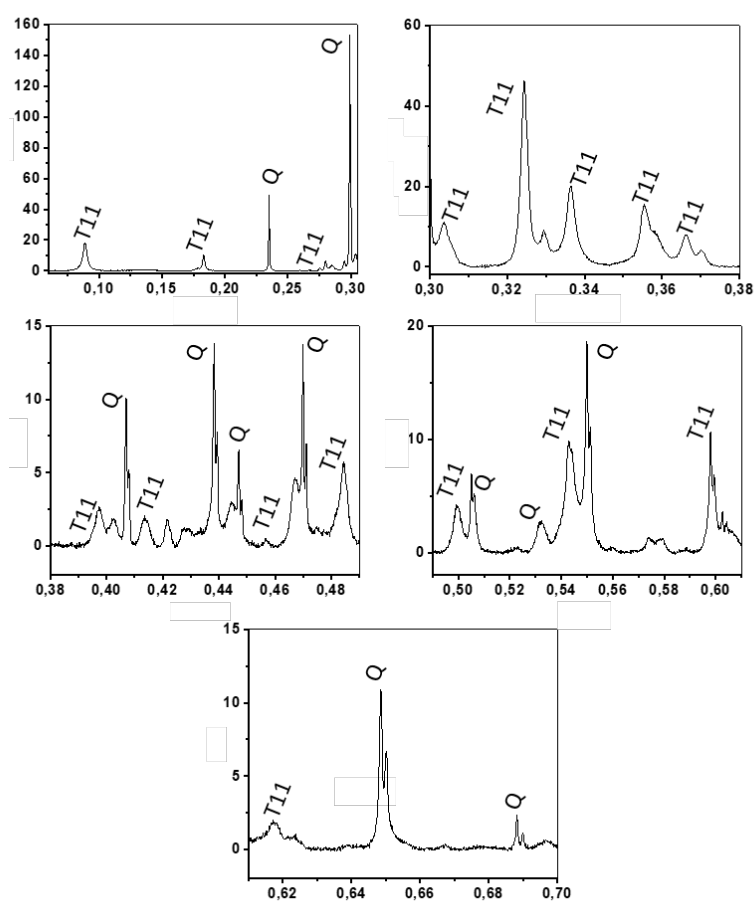


Figure 4.4: (a) Reference XRD survey of fresh tobermorite sample at the room temperature. (b) A comprehensive detail of all phases and the unit cell dimensions. T11: tobermorite 11 Å, Q: Quartz.

To obtain the minimum energy path (MEP), the nudged elastic band (NEB) method is employed, which is a chain-states method in way a string of images is employed. In Figure 4.3, the NEB method demonstrates a barrier-less reaction pathway of formation of CO₃ through the reaction of CO at the surface of tobermorite 11 Å (004). To explain the NEB reaction precisely, Figure 4.3a indicates the initial model of dreierkette silicate chain for deposition of CO at the tobermorite 11 Å (004) surface.

Figures 4.3b-d display the minima energy procedures of the system by approaching CO at the surface of tobermorite 11 Å. In Figure 4.3d can also be seen that CO₃ is not formed before dissociation of interlayer water and it only bonded to one dangling oxygen coordinated to the silicon atom. The ground-state structure was obtained as the interlayer water dissociated, and therefore a hydroxyl group was exchanged by the dangling oxygen from silicon to form 4-fold coordinated silicon and formation of carbonate at the surface of tobermorite (Figure 4.3e). Since the cementitious materials [1] are porous and existing everywhere, the barrier-less reaction pathway of formation of CO₃ through the reaction of CO at the surface of tobermorite illustrates the CO storages in the ambient atmosphere for deleterious and dangerous CO gas formed by the incomplete combustion of fuels. It is also worth reporting that, the high energy of 3.5 eV is needed for reverse reaction from CO₃ to CO formation, which is impossible to take place in the ambient atmosphere. Figure 4.5 also illustrates the unit cell side view for the ground-state structure of tobermorite 11 Å (Figure 4.3e) when the dissociation of interlayer water, the solid-state diffusion, and consequently the formation of carbonate at the surface took place.

We have additionally performed the DFT computational method for the ground-state structure of Figure 4.3e to compute the IR spectra as illustrated in Figure 4.7 to correlate it with NEB. Initially, IR spectra for the ground-state structure of tobermorite 11 Å as the background was measured as shown in Figure 4.6. Then IR spectra for the ground-state structure of tobermorite 11 Å after deposition of CO at the surface of tobermorite 11 Å (004) was plotted in Figure 4.7. As we observed in Figure 4.7, together with the dissociation of interlayer water and the solid-state diffusion for the stretching vibrations of $\nu(\text{Si-OH})$ at 2926, 2505, and 2271 cm⁻¹, the two stretching vibrations of $\nu_{\text{as}}(\text{CO}_3)$ at 1765 and 1318 cm⁻¹ were observed [98].

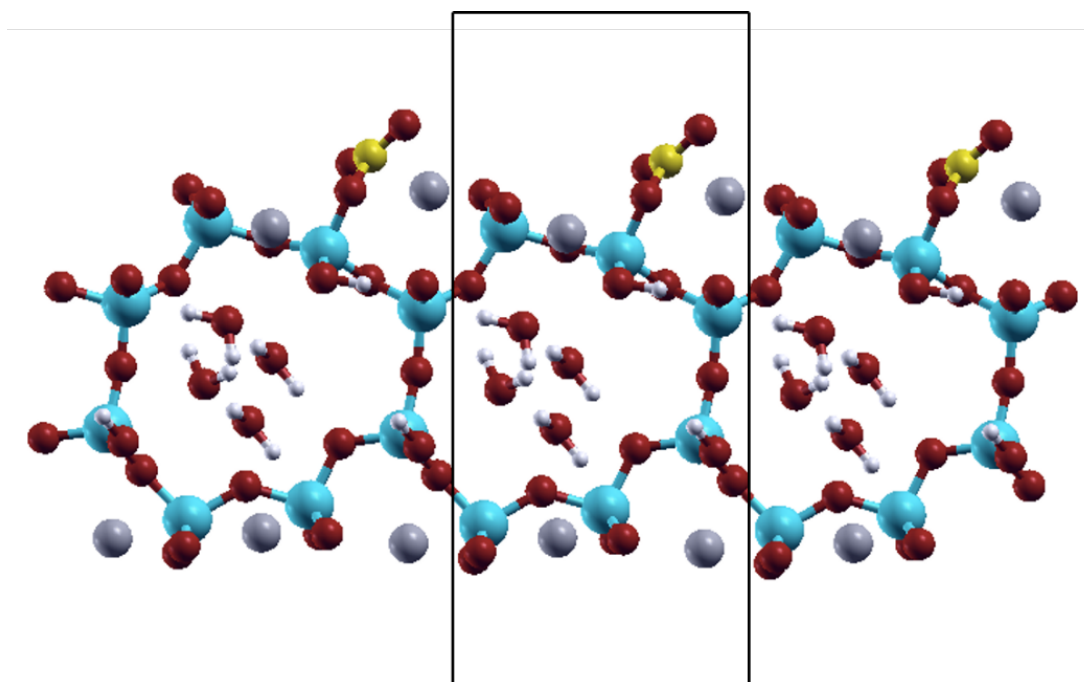


Figure 4.5: The unit cell side view for the ground-state structure of tobermorite 11 Å when the dissociation of interlayer water molecule, solid-state diffusion, and consequently formation of carbonate at the surface took place.

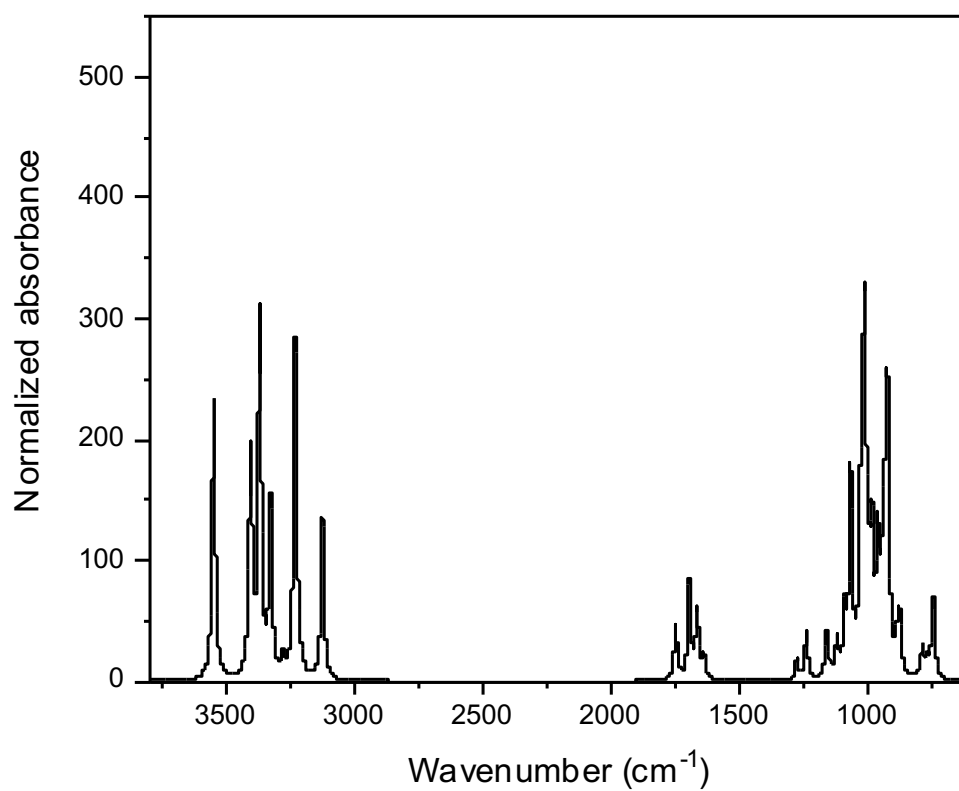


Figure 4.6: IR spectra for the ground-state structure of tobermorite 11 Å as the background.

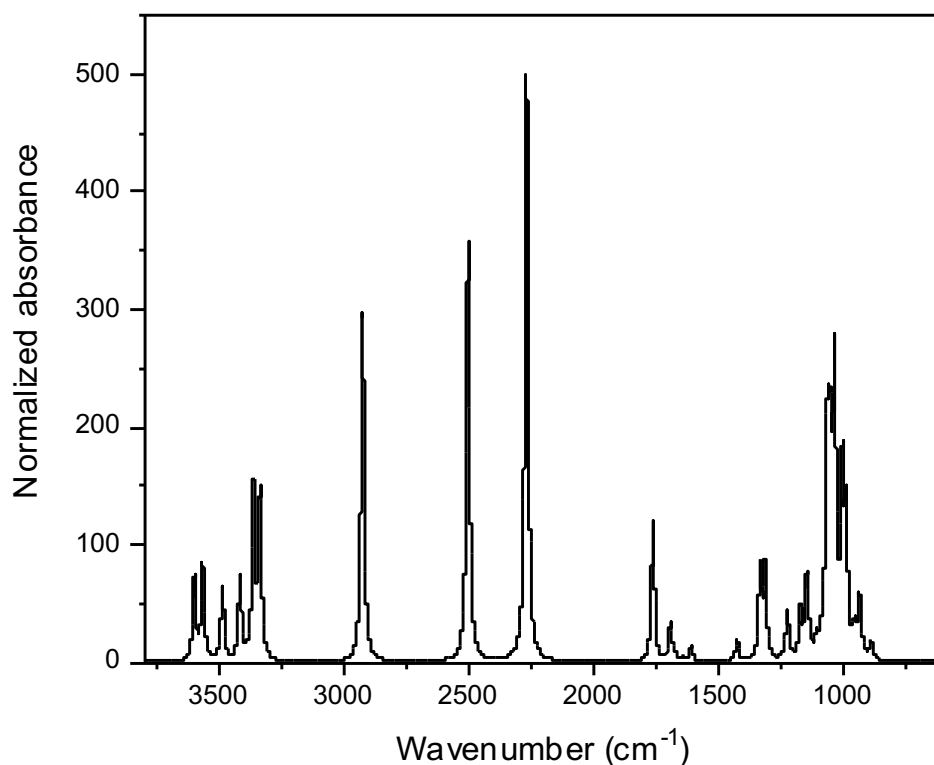


Figure 4.7: IR spectra for the ground-state structure of tobermorite 11 Å after deposition of CO at the surface of tobermorite 11 Å (004) as the interlayer water molecule dissociated, and therefore the carbonate was formed at the surface.

The peaks corresponding to the stretching and bending vibrations of $\nu_{\text{as}}(\text{H-O-H})$ and $\delta(\text{H-O-H})$ were seen at 3599-3336 and 1695-1612 cm^{-1} , respectively. The vibrations of dangling oxygen from silicon chain observed by the stretching peaks of $\nu(\text{Si-O})$ at 1176, 1112, 1094, 1088, 1069, 1059, 1054, 1042, 1009, 995, 992 and 942 cm^{-1} [70]. The stretching vibrations of $\nu_{\text{as}}(\text{Si-O-Si})$ at 1229, 1176, 1155, 1112, 1094, 1042, 1038, 1009, and 995 cm^{-1} were seen. Note that the both stretching peaks of $\nu(\text{Si-O})$ and $\nu_{\text{as}}(\text{Si-O-Si})$ have been observed at 1176, 1155, 1112, 1094, 1042, 1009, and 995 cm^{-1} . An interesting conclusion for carbonate formation at the dry surface with interlayer water can be extracted comparing the IR spectra from experimental method and the ground-state structure obtained through nudged elastic band (NEB), which are in an excellent agreement with each other. Figure 4.8 also illustrates the IR spectra for the ground-state structure of tobermorite 11 Å after deposition of CO at the surface of tobermorite 11 Å (004) subtracted relative to the background spectra. The negative peaks at 3599-3336 demonstrates that the intensity of those peaks were lower after deposition of CO at the surface in comparison to the background, which evidence the dissociation of interlayer water molecules. On the one hand, together with the dissociation of interlayer water and consequently

the new peaks for the stretching vibrations of $\nu(\text{Si-OH})$ at 2926, 2505, and 2271 cm^{-1} were observed. It is also worth mentioning that the intensity of two stretching vibrations of $\nu_{\text{as}}(\text{CO}_3)$ at 1765 and 1318 cm^{-1} were increased after subtraction proving formation of CO_3 at the surface.

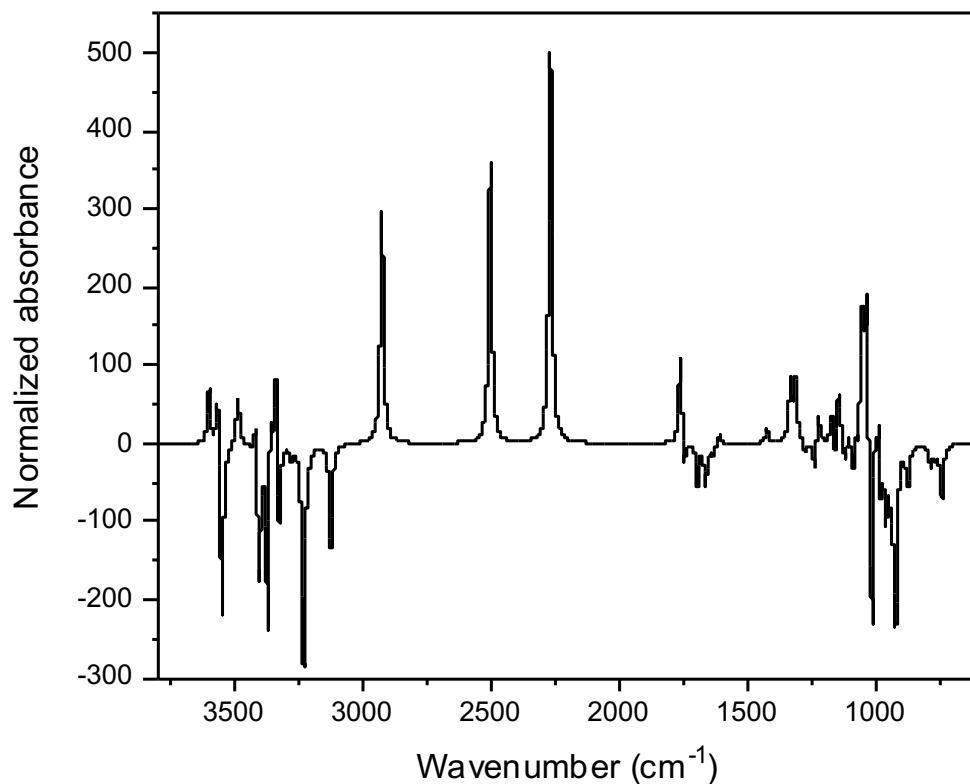


Figure 4.8: IR spectra for the ground-state structure of tobermorite 11 Å after deposition of CO at the surface of tobermorite 11 Å (004) subtracted relative to the background spectra.

4.2 CO₂ Deposition at the Surface of Tobermorite 11 Å (004)

In the second part of this study, we studied the carbonate formation at the surface of tobermorite 11 Å (004) by deposition of CO₂ with supporting DFT calculation of NEB method and FTIR measurements for samples exposed in the ambient atmosphere and heated by thermogravimetric analysis. In this way, a study was carried out to prove the effect of dry and wet mechanism at the surface of mineral with CO₂ absorbent. C. Longo et al. [28] thus reported that a carbonate monolayer has been formed and further reactions stop for the free-water surface of wollastonite (001) with CO₂. They also proved that the reaction of carbonate is strongly affected and completely changed in the presence of water in the ambient atmosphere. Therefore, either water from ambient atmosphere or mineral's surface can accelerate the growth of carbonate formation on the surface. In the present study, our observations by DFT calculation through NEB method proved that CO₂ approaches on the surface of tobermorite 11 Å (004) without changing of the orientation (Figure 4.9a-c). Although CO₂ at the surface of tobermorite 11 Å (004) is adsorbed on the top of dangling oxygen in a slightly tilted orientation for ground-state structure (Figure 4.7d), very little and feasible energy of 0.05 eV is needed to form CO₃ at the surface of tobermorite in the ambient atmosphere (Figure 4.9e).

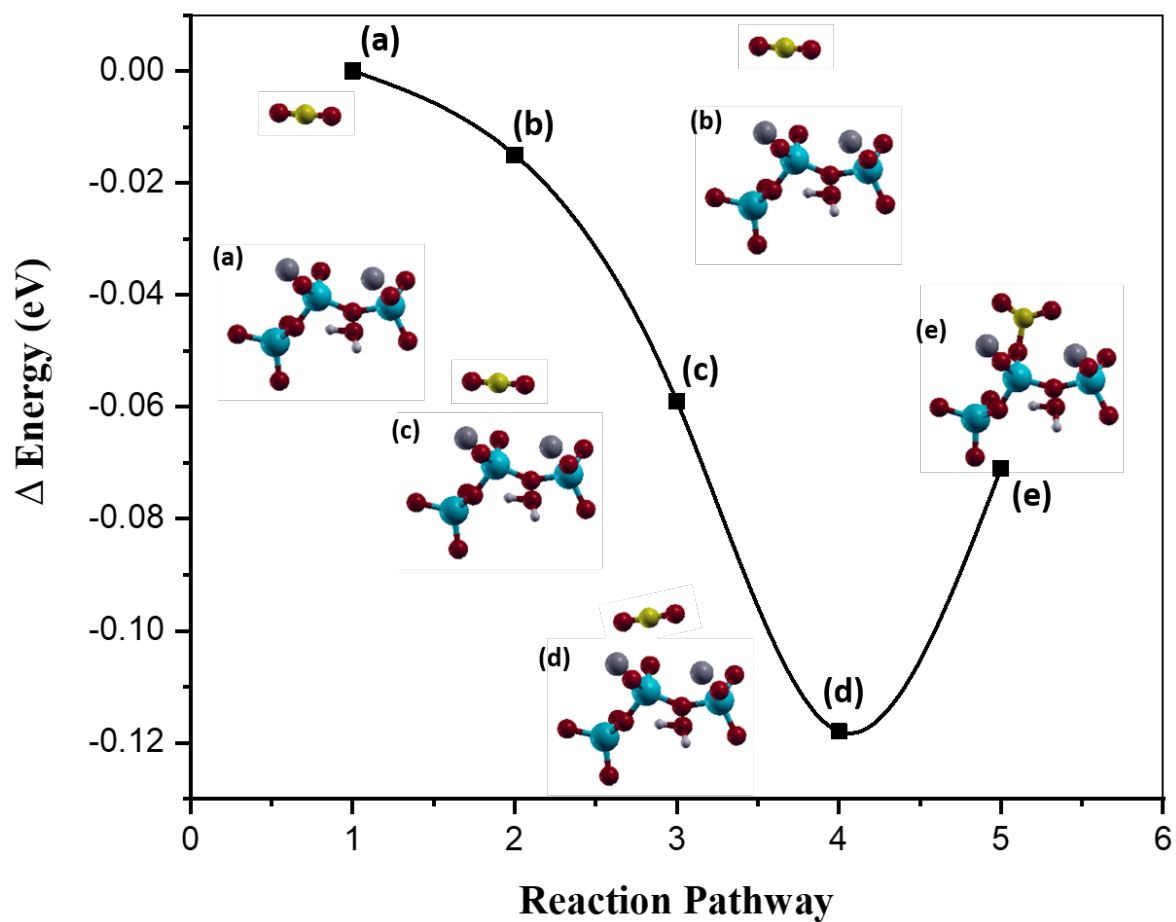


Figure 4.9: The DFT calculation of minimum energy path of CO₂ reacting with the tobermorite 11 Å (004) resulting CO₃ formation at the surface. The light blue atoms represent Si; red, O; gray, Ca; white, H; yellow, C atoms, respectively.

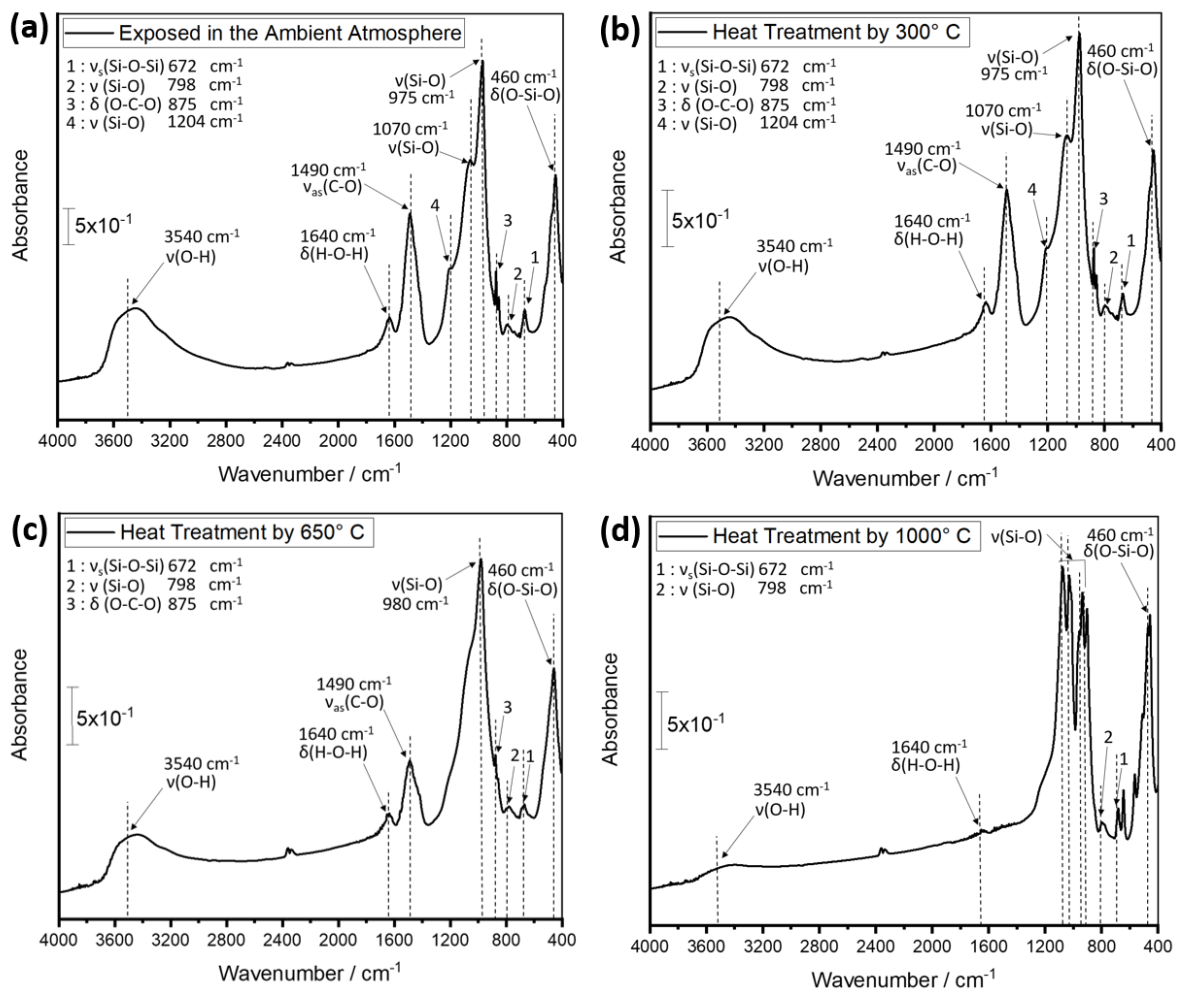


Figure 4.10: (a) FTIR spectra of (CSH) phases referenced to the thin film of tobermorite with KBr exposed in the ambient atmosphere. (b-d) FTIR spectra of (CSH) phases referenced to the thin film of tobermorite with KBr heated up to 300°, 650°, and 1000° C by thermogravimetric analysis.

To demonstrate the formation of CO₃ at the surface by experimental method, FTIR measurement for the thin film of tobermorite combined with KBr exposed in the ambient atmosphere indicates the stretching vibration of $\nu_{\text{as}}(\text{CO}_3)$ at 1490 cm⁻¹ resulting carbonate formation at the surface of tobermorite (Figure 4.10a). Figure 4.10b-d illustrate the FTIR measurement for the identical samples to investigate CO₃ stability, however, heated up to 300°, 650°, and 1000° C by thermogravimetric analysis. Although the intensity of CO₃ remains constant by 300° C, the reverse reaction of CO₃ to CO₂ starts by 650° C as the intensity of CO₃ at 1490 cm⁻¹ decreases. Finally, the total carbonates at the surface of tobermorite were decomposed by 1000° C. Although the formation of CO₃ (Figure 4.9e) from ground-state structure of adsorbed CO₂ at the surface of tobermorite (Figure 4.9d) needs very little energy of 0.05 eV, the converse reaction decomposition of CO₃ to CO₂ requires really external activation energy.

4.3 NO and NO₂ Depositions at the Surface of Tobermorite 11 Å (004)

In the last part of this study, we studied about the possible storage of NO and NO₂, an important toxic industrial pollutant and chemical, from air by possible reactions at the surface of tobermorite within DFT calculation. Y. Chen et al. [99] also studied nitrate (NO₃) formation from capturing toxic gases of NO and NO₂ by promising and environmentally friendly deep eutectic solvents (DESs) method. More recently, G.W. Peterson et al. [100] also studied such high removal of the toxic nitrogen dioxide at extraordinary levels by UiO-66-NH₂. The initial deposition of NO at the surface of tobermorite 11 Å (004) is shown in Figure 4.11a. Figure 4.11b indicates the ground-state structure, which was obtained as the interlayer water molecule dissociated, and consequently hydroxyl group exchanged by dangling oxygen from silicon to form 4-fold coordinated silicon; and finally, formation of NO₂ at the surface of tobermorite with the adsorption energy of -0.4503 eV. We moreover deposited NO₂ at the surface of tobermorite 11 Å (004) to observe the further reaction (Figure 4.12a). As shown in Figure 4.12b, NO₂ can be stored at the surface of tobermorite for the ground-state structure by the formation of nitrate (NO₃). Therefore, because of formation of NO₂ from NO (Figure 4.11), we can on the one hand conclude that nitrate formation at the tobermorite surface is also valid for NO deposition.

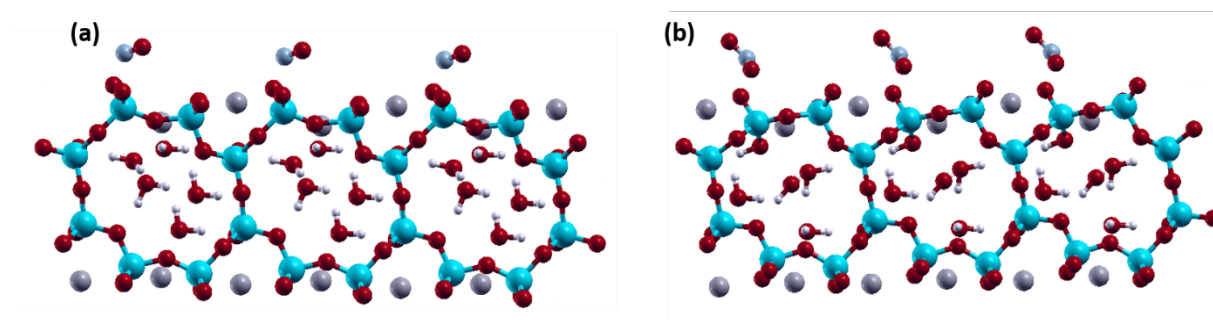


Figure 4.11: (a) The unit cell side view as NO is deposited at the surface of tobermorite 11 Å. (b) The ground-state structure as the interlayer water dissociated resulting creation of NO₂ at the surface of tobermorite 11 Å.

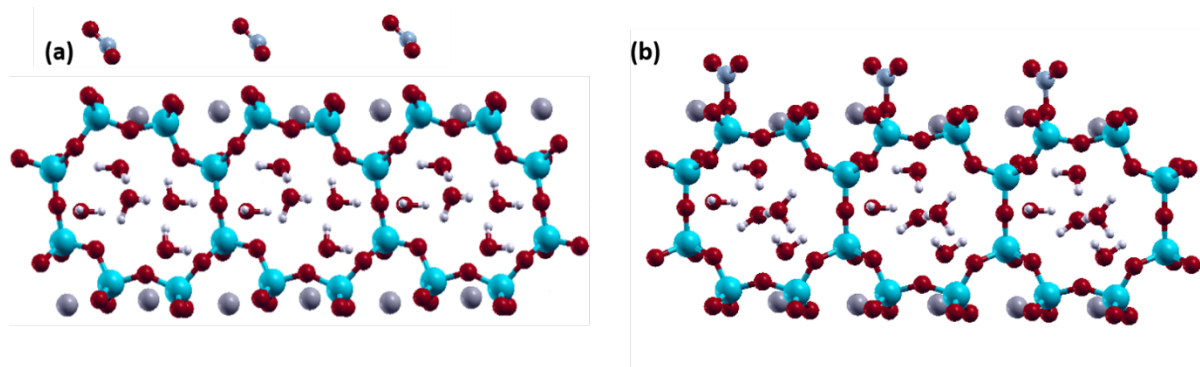


Figure 4.12: (a) The unit cell side view as NO₂ is deposited at the surface of tobermorite 11 Å. (b) The ground-state structure as carbonate is formed at the surface of tobermorite 11 Å.

4.4 Summary

In summary, we have evidenced the possible storage of carbon monoxide (CO), carbon dioxide (CO₂), nitric oxide (NO), and nitrogen dioxide (NO₂) at the surface of tobermorite 11 Å (004) within the nudged elastic band (NEB) by DFT calculation and FTIR measurement. The DFT calculation and FTIR measurement methods demonstrate that the growth of carbonate at the surface of tobermorite happens together with the dissociation of interlayer water molecule for CO deposition at the surface of tobermorite. Although the NEB methods demonstrate a barrierless reaction pathway of formation of CO₃ through the reaction of CO at the surface of tobermorite, little energy of 0.05 eV is needed to be formed the carbonate for CO₂ deposition. Nevertheless, we have shown through FTIR measurement that the carbonate is formed for CO₂ deposition at the surface of tobermorite as it is exposed in the ambient atmosphere. It was also reported that the capturing toxic gases of NO and NO₂ can be carried out by nitrate formation at the tobermorite surface.

Concluding Remarks

Below are summarized the main conclusions of the three projects developed in this dissertation.

Correlation between Composition and Mechanical Properties of Calcium Silicate Hydrates Identified by Infrared Spectroscopy and Density Functional Theory: Through DFT calculation method, we have successfully simulated the eight various calcium silicate (CS) and calcium silicate hydrate (CSH) phases as our model system, such as tobermorite 14 Å, tobermorite 11 Å, tobermorite 9 Å, wollastonite, jaffeite, jennite, γ -C₂S, and α -C₂SH, which are produced during hydration of cement. Then, in order to measure the compressibility of the phases, the bulk modulus of all phases were computed as the function of C/S ratio. In fact, the presence of water molecules inside the structure of each phase was identified as one of the fundamental parameters. The bulk modulus of all phases was computed and jaffeite, γ -C₂S, and α -C₂SH were combined in isotropic models. The monomer structure of silicate tetrahedra was found in jaffeite, γ -C₂S, and α -C₂SH. tobermorite 14 Å and γ -C₂S represent the lowest and highest bulk modulus, respectively. The calculated IR spectra of (CS) and (CSH) phases for four vibration modes of asymmetrical and symmetrical stretching and bending based on the two criteria of the H/C and C/S ratios identified within DFT calculation. A global trend for the wavenumber of $\nu(\text{Si-O})$ in (CS) and (CSH) phases was not manifested but we recommended that as H/C ratios increase for identical C/S ratio, the wavenumbers of $\nu(\text{Si-O})$ decrease as well. Furthermore, the wavenumbers of $\nu(\text{Si-O})$ increase for the identical H/C ratio as C/S ratios increase.

Interaction of Reduced Graphene Oxide with Monomers of (Calcium) Silicate Hydrates: A First-Principles Study: Through DFT computational method, we used reduced graphene oxide (rGO) to be involved with calcium silicate hydrated (CSH) moieties to make new nanocomposite materials. It is significant to employ two-dimensional material with exceptional mechanical, electrical and thermal properties to be used in nanocomposites. By exfoliation and oxidation of graphite, reduced graphene oxide (rGO) sheet is produced and mainly coated by surface functional groups of hydroxyl and epoxide. In our study, we performed a comprehensive examination for the interaction mechanism of rGO having epoxy and hydroxyl groups with related (CSH) moieties given by monomers of silicate tetrahedra, and Ca. One significant information is that, the interaction of hydroxyl/rGO with silicate tetrahedra

can selectively repair the hydroxyl defects on the rGO lattice back into the graphene. Moreover, repulsion of defect from graphene sheet, and consequently condensation reaction even took place in the presence of Ca and hydroxyl groups. This might open interesting wet-chemical solutions for the future in the field of nanocomposites involving functional properties different from mechanical ones. On the contrary, the ground-state structure remains closely to the initial structure model for the interaction of epoxide/rGO with (CSH) gel. In this case, strong interactions have been examined for the composite materials design. Furthermore, the electronic properties for some calculated ground-state structures was examined through DOS and Bader charge analysis. It was found that the Fermi level was located below the charge neutrality point of the graphene layer, being positively charged in a system consisting of Si(OH)₃, water and graphene sheet. On the contrary, in the same system with contribution of Ca, the Fermi level was located above the charge neutrality point of the graphene layer, being negatively charged.

Capture of Toxic Gases by Cementitious Components: In this project, within the nudged elastic band (NEB) through DFT calculation method and FTIR measurement, we derived the possible storages of carbon monoxide (CO), carbon dioxide (CO₂), nitric oxide (NO), and nitrogen dioxide (NO₂) gases at the surface of tobermorite 11 Å (004). We indeed selected tobermoriet 11 Å because the majority of measured tobermorite through X-ray diffraction (XRD) method was detected from type of 11 Å. The surface orientation of (004) with the lowest surface energy of 0.41 J/m² was reported as the most stable surface for the tobermorite 11 Å. For CO deposition at the surface of tobermorite, the grows of carbonate at the surface of tobermorite happens together with the dissociation of interlayer water molecule. Even though the barrier-less reaction pathway of formation of CO₃ were demonstrated by the NEB method through the reaction of CO at the surface of tobermorite, little energy of 0.05 eV was required to get the formation of carbonate for CO₂ deposition at the surface of tobermorite. Nonetheless, it was shown that carbonate is formed for CO₂ deposition at the surface of tobermorite as it is exposed in the ambient atmosphere through FTIR measurement. By heating treatment, the only toxic gas of CO is remained, and decomposition process of CO₂ from carbonate is the only reverse possible reaction due to the little energy of 0.05 eV as evidenced through NEB. We have also shown that toxic gases of NO, and NO₂ can be captured by cementitious components as it was performed at the surface of tobermorite 11 Å (004) within DFT calculation.

Bibliography

1. Izadifar, M., et al., *Correlation between composition and mechanical properties of calcium silicate hydrates identified by infrared spectroscopy and density functional theory*. The Journal of Physical Chemistry C, 2019. **123**(17): p. 10868-10873.
2. Abdolhosseini Qomi, M.J., et al., *Combinatorial molecular optimization of cement hydrates*. Nature Communications, 2014. **5**(1): p. 4960.
3. Worrell, E., et al., *Carbon dioxide emissions from the global cement industry*. Annual Review of Energy and the Environment, 2001. **26**(1): p. 303-329.
4. Collepardi, M., *Admixtures used to enhance placing characteristics of concrete*. Cement and Concrete Composites, 1998. **20**(2): p. 103-112.
5. Gagg, C.R., *Cement and concrete as an engineering material: An historic appraisal and case study analysis*. Engineering Failure Analysis, 2014. **40**: p. 114-140.
6. Allen, A.J., et al., *Composition and density of nanoscale calcium-silicate-hydrate in cement*. Nat Mater, 2007. **6**(4): p. 311-6.
7. Dolado, J.S., et al., *A molecular dynamic study of cementitious calcium silicate hydrate (C-S-H) gels*. Journal of the American Ceramic Society, 2007. **90**(12): p. 3938-3942.
8. Pellenq, R.J.M., et al., *A realistic molecular model of cement hydrates*. Proceedings of the National Academy of Sciences, 2009. **106**(38): p. 16102-16107.
9. Skinner, L.B., et al., *Nanostructure of calcium silicate hydrates in cements*. Physical Review Letters, 2010. **104**(19): p. 195502.
10. Manzano, H., et al., *Confined water dissociation in microporous defective silicates: mechanism, dipole distribution, and impact on substrate properties*. Journal of the American Chemical Society, 2012. **134**(4): p. 2208-2215.
11. Sanna, S., et al., *Formation of hydroxyl groups at calcium-silicate-hydrate (C-S-H): coexistence of Ca-OH and Si-OH on wollastonite(001)*. The Journal of Physical Chemistry C, 2014. **118**(15): p. 8007-8013.
12. Andrew, R.M., *Global CO₂ emissions from cement production*. Earth Syst. Sci. Data, 2018. **10**(1): p. 195-217.
13. Giraudo, N., et al., *Corrosion of concrete by water-induced metal-proton exchange*. The Journal of Physical Chemistry C, 2016. **120**(39): p. 22455-22459.
14. Thissen, P., *Exchange reactions at mineral interfaces*. Langmuir, 2020. **36**(35): p. 10293-10306.
15. Ebbert, C., et al., *Toward a microscopic understanding of the calcium-silicate-hydrates/water interface*. Applied Surface Science, 2014. **290**: p. 207.
16. Richardson, I.G., *The nature of the hydration products in hardened cement pastes*. Cement and Concrete Composites, 2000. **22**(2): p. 97-113.
17. Hou, D., et al., *Uniaxial tension study of calcium silicate hydrate (C-S-H): structure, dynamics and mechanical properties*. Materials and Structures, 2015. **48**(11): p. 3811-3824.
18. Bauchy, M., et al., *Fracture toughness of calcium-silicate-hydrate from molecular dynamics simulations*. Journal of Non-Crystalline Solids, 2015. **419**: p. 58-64.
19. Vandamme, M., et al., *Nanogranular origin of concrete creep*. Proceedings of the National Academy of Sciences of the United States of America, 2009. **106**(26): p. 10552-10557.
20. Dolado, J.S., et al., *A molecular dynamic study of cementitious calcium silicate hydrate (C-S-H) gels*. Journal of the American Ceramic Society, 2007. **90**(12): p. 3938-3942.
21. Masoumi, S., et al., *Effective Interactions Between Calcium-Silicate-Hydrate Nanolayers*. The Journal of Physical Chemistry C, 2019.
22. Richardson, I.G., *The calcium silicate hydrates*. Cement and Concrete Research, 2008. **38**(2): p. 137-158.
23. Pellenq, R.J.M., et al., *A realistic molecular model of cement hydrates*. Proceedings of the National Academy of Sciences of the United States of America, 2009. **106**(38): p. 16102-16107.
24. Jennings, H.M., *Refinements to colloid model of C-S-H in cement: CM-II*. Cement and Concrete Research, 2008. **38**(3): p. 275-289.

25. González-Teresa, R., et al., *Nanoscale texture development of C-S-H gel: A computational model for nucleation and growth*. Applied Physics Letters, 2013. **103**(23): p. 234105.
26. Prabhu, A., et al., *A multi-scale approach for percolation transition and its application to cement setting*. Scientific Reports, 2018. **8**(1): p. 15830.
27. Ioannidou, K., et al., *Mesoscale texture of cement hydrates*. Proceedings of the National Academy of Sciences, 2016. **113**(8): p. 2029-2034.
28. Longo, R.C., et al., *Carbonation of wollastonite(001) competing hydration: microscopic insights from ion spectroscopy and density functional theory*. ACS Applied Materials & Interfaces, 2015. **7**(8): p. 4706-4712.
29. Morshedifard, A., et al., *Nanoscale origins of creep in calcium silicate hydrates*. Nature Communications, 2018. **9**.
30. Thissen, P., et al., *Hydration of concrete: The first steps*. Chemistry – A European Journal, 2018. **24**(34): p. 8603-8608.
31. Giraud, N., et al., *Early stage hydration of wollastonite: kinetic aspects of the metal-proton exchange reaction*. The Journal of Physical Chemistry C, 2015. **119**(19): p. 10493-10499.
32. Oelkers, E.H., et al., *The surface chemistry of multi-oxide silicates*. Geochimica et Cosmochimica Acta, 2009. **73**(16): p. 4617-4634.
33. Giraud, N., et al., *Passivation of hydrated cement*. ACS Sustainable Chemistry & Engineering, 2018. **6**(1): p. 727-737.
34. Novoselov, K.S., et al., *Electric field effect in atomically thin carbon films*. Science, 2004. **306**(5696): p. 666-669.
35. Wu, D., et al., *Nanocomposites and macroscopic materials: assembly of chemically modified graphene sheets*. Chemical Society Reviews, 2012. **41**(18): p. 6160-6177.
36. Parvez, K., et al., *Nitrogen-doped graphene and its iron-based composite as efficient electrocatalysts for oxygen reduction reaction*. ACS Nano, 2012. **6**(11): p. 9541-9550.
37. Wu, Z.S., et al., *Graphene-based in-plane micro-supercapacitors with high power and energy densities*. Nature Communications, 2013. **4**(1): p. 2487.
38. Bae, S., et al., *Roll-to-roll production of 30-inch graphene films for transparent electrodes*. Nature Nanotechnology, 2010. **5**(8): p. 574-578.
39. Balandin, A.A., et al., *Superior thermal conductivity of single-layer graphene*. Nano Letters, 2008. **8**(3): p. 902-907.
40. Mortazavi, B., et al., *Multiscale modeling of heat conduction in graphene laminates*. Carbon, 2015. **85**: p. 1-7.
41. Mortazavi, B., et al., *Multiscale modeling of thermal conductivity of polycrystalline graphene sheets*. Nanoscale, 2014. **6**(6): p. 3344-3352.
42. Izadifar, M., et al., *Nanopores creation in boron and nitrogen doped polycrystalline graphene: A molecular dynamics study*. Physica E: Low-dimensional Systems and Nanostructures, 2018. **99**: p. 24-36.
43. Williams, J.R., et al., *Quantum hall effect in a gate-controlled junction of graphene*. Science, 2007. **317**(5838): p. 638-641.
44. Lee, C., et al., *Measurement of the elastic properties and intrinsic strength of monolayer graphene*. Science, 2008. **321**(5887): p. 385-388.
45. Mortazavi, B., et al., *Atomistic modeling of mechanical properties of polycrystalline graphene*. Nanotechnology, 2014. **25**(21): p. 215704.
46. Geim, A.K., et al., *The rise of graphene*. Nature Materials, 2007. **6**(3): p. 183-191.
47. Park, S., et al., *Chemical methods for the production of graphenes*. Nature Nanotechnology, 2009. **4**(4): p. 217-224.
48. Parvez, K., et al., *Exfoliation of graphite into graphene in aqueous solutions of inorganic salts*. Journal of the American Chemical Society, 2014. **136**(16): p. 6083-6091.
49. Izadifar, M., et al., *Fracture toughness of various percentage of doping of boron atoms on the mechanical properties of polycrystalline graphene: A molecular dynamics study*. Physica E: Low-dimensional Systems and Nanostructures, 2019. **114**: p. 113614.
50. Sutter, P.W., et al., *Epitaxial graphene on ruthenium*. Nat Mater, 2008. **7**(5): p. 406-11.
51. Lee, Y., et al., *Wafer-scale synthesis and transfer of graphene films*. Nano Lett, 2010. **10**(2): p. 490-3.

52. Eigler, S., et al., *Wet chemical synthesis of graphene*. *Advanced Materials*, 2013. **25**(26): p. 3583-3587.
53. Niu, L., et al., *Salt-assisted direct exfoliation of graphite into high-quality, large-size, few-layer graphene sheets*. *Nanoscale*, 2013. **5**(16): p. 7202-7208.
54. Chua, C.K., et al., *Chemical reduction of graphene oxide: a synthetic chemistry viewpoint*. *Chemical Society Reviews*, 2014. **43**(1): p. 291-312.
55. Hummers, W.S., et al., *Preparation of graphitic oxide*. *Journal of the American Chemical Society*, 1958. **80**(6): p. 1339-1339.
56. Chen, J., et al., *Water-enhanced oxidation of graphite to graphene oxide with controlled species of oxygenated groups*. *Chemical Science*, 2016. **7**(3): p. 1874-1881.
57. Zhao, J., et al., *Synthesis of thermally reduced graphite oxide in sulfuric acid and its application as an efficient lubrication additive*. *Tribology International*, 2017. **116**: p. 303-309.
58. Jung, I., et al., *Simple approach for high-contrast optical imaging and characterization of graphene-based sheets*. *Nano Letters*, 2007. **7**(12): p. 3569-3575.
59. Stankovich, S., et al., *Stable aqueous dispersions of graphitic nanoplatelets via the reduction of exfoliated graphite oxide in the presence of poly(sodium 4-styrenesulfonate)*. *Journal of Materials Chemistry*, 2006. **16**(2): p. 155-158.
60. Acik, M., et al., *Unusual infrared-absorption mechanism in thermally reduced graphene oxide*. *Nature Materials*, 2010. **9**(10): p. 840-845.
61. Feng, H., et al., *A low-temperature method to produce highly reduced graphene oxide*. *Nature Communications*, 2013. **4**(1): p. 1539.
62. Liao, K.-H., et al., *Aqueous only route toward graphene from graphite oxide*. *ACS Nano*, 2011. **5**(2): p. 1253-1258.
63. Pei, S., et al., *Direct reduction of graphene oxide films into highly conductive and flexible graphene films by hydrohalic acids*. *Carbon*, 2010. **48**(15): p. 4466-4474.
64. Li, W., et al., *Effects of nanoalumina and graphene oxide on early-age hydration and mechanical properties of cement paste*. *Journal of Materials in Civil Engineering*, 2017. **29**(9): p. 04017087.
65. Gong, K., et al., *Reinforcing effects of graphene oxide on portland cement paste*. *Journal of Materials in Civil Engineering*, 2015. **27**(2): p. A4014010.
66. Jyothimol, P., et al., *Effect of reduced graphene oxide on the mechanical properties of concrete*. *IOP Conference Series: Earth and Environmental Science*, 2020. **491**: p. 012038.
67. Kresse, G., et al., *Ab initio molecular dynamics for liquid metals*. *Physical Review B*, 1993. **47**(1): p. 558-561.
68. Kresse, G., et al., *Efficient iterative schemes for ab initio total-energy calculations using a plane-wave basis set*. *Physical Review B*, 1996. **54**(16): p. 11169-11186.
69. Kresse, G., et al., *Efficiency of ab-initio total energy calculations for metals and semiconductors using a plane-wave basis set*. *Computational Materials Science*, 1996. **6**(1): p. 15-50.
70. Giraud, N., et al., *Calcium silicate phases explained by high-temperature-resistant phosphate probe molecules*. *Langmuir*, 2016. **32**(51): p. 13577-13584.
71. Perdew, J.P., et al., *Generalized gradient approximation made simple*. *Physical Review Letters*, 1996. **77**(18): p. 3865-3868.
72. Kresse, G., et al., *From ultrasoft pseudopotentials to the projector augmented-wave method*. *Physical Review B*, 1999. **59**(3): p. 1758-1775.
73. Monkhorst, H.J., et al., *Special points for Brillouin-zone integrations*. *Physical Review B*, 1976. **13**(12): p. 5188-5192.
74. Henkelman, G., et al., *A fast and robust algorithm for Bader decomposition of charge density*. *Computational Materials Science*, 2006. **36**(3): p. 354-360.
75. Kresse, G., et al., *Ab initio force constant approach to phonon dispersion relations of diamond and graphite*. *Europhysics Letters (EPL)*, 1995. **32**(9): p. 729-734.
76. Kokalj, A., *XCrySDen—a new program for displaying crystalline structures and electron densities*. *Journal of Molecular Graphics and Modelling*, 1999. **17**(3): p. 176-179.
77. Mutisya, S.M., et al., *The surface stability and morphology of tobermorite 11 Å from first principles*. *Applied Surface Science*, 2018. **444**: p. 287-292.
78. Bonaccorsi, E., et al., *The crystal structure of tobermorite 14 Å (Plombierite), a C–S–H phase*. *Journal of the American Ceramic Society*, 2005. **88**(3): p. 505-512.

79. Maeshima, T., et al., *Natural 1.1 and 1.4 nm tobermorites from Fuka, Okayama, Japan: Chemical analysis, cell dimensions, ²⁹Si NMR and thermal behavior*. Cement and Concrete Research, 2003. **33**(10): p. 1515-1523.
80. Hamid, S.A., *The crystal structure of the 11Å natural tobermorite Ca_{2.25}[Si₃O_{7.5}(OH)_{1.5}] · 1H₂O*. Zeitschrift für Kristallographie - Crystalline Materials, 1981. **154**(3-4): p. 189.
81. Megaw, H.D., et al., *Crystal structure of tobermorite*. Nature, 1956. **177**(4504): p. 390-391.
82. Kundu, T.K., et al., *Atomistic simulation of the surface structure of wollastonite*. Chemical Physics Letters, 2003. **377**(1): p. 81-92.
83. Churakov, S.V., *Hydrogen bond connectivity in jennite from ab initio simulations*. Cement and Concrete Research, 2008. **38**(12): p. 1359-1364.
84. Bonaccorsi, E., et al., *The crystal structure of jennite, Ca₉Si₆O₁₈(OH)₆·8H₂O*. Cement and Concrete Research, 2004. **34**(9): p. 1481-1488.
85. Carpenter, A.B., et al., *Jennite, a new mineral*. American Mineralogist, 1966. **51**(1-2): p. 56-74.
86. Garbev, K., et al., *A Modular concept of crystal structure applied to the thermal transformation of α-C₂SH*. Journal of the American Ceramic Society, 2014. **97**(7): p. 2286-2297.
87. Garbev, K., et al., *Preparation of a novel cementitious material from hydrothermally synthesized C-S-H phases*. Journal of the American Ceramic Society, 2014. **97**: p. 2298-2307.
88. Hirose, K., et al., *Stability and equation of state of MgGeO₃ post-perovskite phase*. American Mineralogist, 2005. **90**(1): p. 262-265.
89. Manzano, H., et al., *Mechanical properties of crystalline calcium-silicate-hydrates: comparison with cementitious C-S-H gels*. physica status solidi (a), 2007. **204**(6): p. 1775-1780.
90. Walker, C.S., et al., *Non-ideal solid solution aqueous solution modeling of synthetic calcium silicate hydrate*. Cement and Concrete Research, 2007. **37**(4): p. 502-511.
91. Qin, W., et al., *Density functional theory calculations and molecular dynamics simulations of the adsorption of biomolecules on graphene surfaces*. Biomaterials, 2010. **31**(5): p. 1007-1016.
92. Guo, Y.n., et al., *Density functional theory study of the interaction of arginine-glycine-aspartic acid with graphene, defective graphene, and graphene oxide*. The Journal of Physical Chemistry C, 2013. **117**(11): p. 5708-5717.
93. Fan, X.F., et al., *Interaction between graphene and the surface of SiO₂*. Journal of Physics: Condensed Matter, 2012. **24**(30): p. 305004.
94. Stibor, A., et al., *Density functional study of the adsorption of CO on Fe(110)*. Surface Science, 2002. **507-510**: p. 99-102.
95. Vogt, J., et al., *The structure of carbon monoxide adsorbed on the NaCl(100) surface—A combined LEED and DFT-D/vdW-DF study*. The Journal of Chemical Physics, 2014. **141**(21): p. 214708.
96. Eren, B., et al., *Carbon monoxide adsorption on manganese oxide/cobalt: an ambient pressure X-ray photoelectron spectroscopy study*. The Journal of Physical Chemistry C, 2020. **124**(6): p. 3557-3563.
97. Hafshejani, T.M., et al., *CO adsorption on the calcite(10.4) surface: a combined experimental and theoretical study*. Physical Chemistry Chemical Physics, 2020. **13**(23): p. 7697-7702.
98. Giraud, N., et al., *Carbonation competing functionalization on calcium-silicate-hydrates: Investigation of four promising surface-activation techniques*. ACS Sustainable Chemistry & Engineering, 2016. **4**(7): p. 3985-3994.
99. Chen, Y., et al., *Capture of toxic gases by deep eutectic solvents*. ACS Sustainable Chemistry & Engineering, 2020. **8**(14): p. 5410-5430.
100. Peterson, G.W., et al., *Extraordinary NO₂ removal by the metal-organic framework UiO-66-NH₂*. Angewandte Chemie International Edition, 2016. **55**(21): p. 6235-6238.